UNIVERSITY OF OSLO
Department of Physics

Electrical transport mechanisms in hydrothermal ZnO

A Hall effect study of lithium's contribution to the ionized impurity electron scattering

Master thesis

Magnus Kvalbein

June 2010

How much better is it to get wisdom than gold. And to get understanding rather to be chosen than silver.

Proverbs XVI, 16

Abstract

Hydrothermal n-type ZnO samples, post-growth annealed in air in the temperature interval 1100-1500 °C, have been investigated by Temperature Dependent Hall effect measurements (TDH), Thermal Admittance Spectroscopy (TAS) and Secondary Ion Mass Spectrometry (SIMS). The bulk Li concentration was found to decrease with increasing annealing temperatures, and was reduced from $9.5 \times 10^{16} cm^{-3}$ to $1.1 \times 10^{15} cm^{-3}$ after the 1100 °C and 1500 °C treatments respectively.

The electron mobility at room temperature (μ_{RT}) and the peak electron mobility (μ_{peak}) showed a large increase as a result of the 1500 °C anneal, reaching a maximum of $\mu_{peak} = 843 cm^2/Vs$ compared to $\mu_{peak} \leq 200 cm^2/Vs$ for the samples annealed at temperatures in the the 1100-1300 °C range. It was found that the distinct increase in mobility was caused by the out-diffusion of an acceptor other than Li_{Zn}, which was believed to be the dominant acceptor in the samples. The identity of this dominating acceptor remains unknown, but V_{Zn} was tentatively suggested.

An increase in charge carrier concentration was observed as a result of higher annealing temperatures and longer annealing times up to 1300 °C. This was mainly due to the formation of a donor with an activation energy of $\sim 30 meV$. This donor's concentration, along with the dominant acceptor's, was reduced after the 1500 °C post-growth anneal.

Acknowledgments

A master thesis is seldom a one man job, and neither is this one. Many others have contributed in many ways, and I am very grateful to all of you.

First of all, I would like to thank my supervisor Prof. Bengt Gunnar Svensson who introduced me to the field of semiconductor physics a few years back. He has mentored me through the work on this thesis in an excellent manner, I always left your office with a little more confidence in this project than when I entered it.

Fortunately we do not have a Hall measurement setup here in Oslo yet. This gave me the opportunity to go to the Royal Institute of Technology (KTH) in Stockholm and to the University of Pretoria (UoP) in South Africa to do most of the measurements. My warm thanks go to the Solid State Electronincs group at KTH, especially Mohammad Usman, for all their help and patience, and to Prof Danie Auret, Wilbert Mtangi, Louwrens van Schallwyk, Johan Janse van Rensburg, Hannes de Meyer and all the others at the Department of Physics at UoP for being great hosts and supervisors during my visit.

I would also like thank all my co-workers at MiNa lab in Oslo, especially Vincent Quemer and Dr Lasse Vines for all their assistance with measurements and sample preparation, and Viktor Bobal for introducing me to the clean room and using the equipment there. A warm thank you goes to Dr Ramon Schifano for letting me use his Matlab script, genuine interest in the results, fruitful discussions and help on interpreting Hall data, and for giving many valuable comments on my thesis. Thanks also to my good friend Halvard Haug for giving me ‘the look’ when turning up at my desk later than 9 am, for carefully proof-reading parts of my thesis, and for all the good times inside and outside of the university campus in the past five years.

My family also needs to be thanked properly, especially my wife Magnhild for being supportive through all the hard work - you're the best. A special thanks goes to my niece Karoline, for reminding me that there are many more fun things to life than semiconductors, like flying kites on a sunny Saturday afternoon.

Financial support by the Norwegian Research Council through a bilateral Norwegian - South African research program is greatly acknowledged.

Contents

Abstract iii

Acknowledgments v

1 Introduction and goal 1

2 Background 3
- 2.1 Basic material and semiconductor theory 3
  - 2.1.1 Crystallography 3
  - 2.1.2 Semiconductors 5
  - 2.1.3 Junctions and contacts in semiconductors 13
- 2.2 Zinc oxide 17
  - 2.2.1 Structural properties of zinc oxide 17
  - 2.2.2 Synthesis of single crystal ZnO 17
  - 2.2.3 Defects and doping of ZnO 19
- 2.3 Previous work 22

3 Experimental methods 27
- 3.1 Annealing 27
- 3.2 Four-point resistivity measurements 28
- 3.3 Secondary Ion Mass Spectrometry 29
- 3.4 Thermal admittance spectroscopy 31
- 3.5 Hall effect measurements 35
  - 3.5.1 Basic relations 35
  - 3.5.2 Temperature dependent Hall effect analysis 39
  - 3.5.3 The Hall scattering factor 41

3.5.4 Curve fitting and theoretical estimations 42
3.5.5 Other galvanomagnetic effects 47
3.5.6 Strengths and weaknesses 47

4 Experimental details and results 49
4.1 Predictions 49
4.2 Sample details 51
4.3 Sample preparation 51
4.3.1 Hall samples 51
4.3.2 TAS samples 55
4.3.3 SIMS samples 55
4.4 Resistivity measurements 56
4.5 TDH results 56
4.6 TAS results 59
4.7 SIMS results 61
4.8 Fitting of TDH data 64

5 Discussion 73
5.1 Li concentration and mobility 73
5.2 Origin and effects of the surface conduction 79
5.3 The Li and Al Diffusion correlation 82
5.4 Suggestions for future studies 84

6 Conclusion and summary 87

Chapter 1

Introduction and goal

The largest challenge of our generation may be global warming and its consequences. It seems beyond doubt that our emission of CO_2 and other greenhouse gases is causing, or at least accelerating, the climate change we are beginning to experience. Novel semiconductors, like zinc oxide (ZnO), may play an important part in producing clean energy through the next generation photovoltaics (PV). In these applications ZnO may act as an active layer in a multi-junction solar cell, or as an transparent conducting front contact on conventional and thin film cells [1].

Semiconductors are also vital in energy efficient light sources, such as light emitting diodes (LEDs), which are increasing their market share as a domestic and industrial light source. Zinc oxide's wide band gap makes it ideal for making devices emitting white light. However, the use of ZnO is not restricted to the applications mentioned above. Zinc oxide has a direct band gap ($\sim$3.37eV) and a large exciton binding energy (60 meV), which makes it possible to develop room temperature exciton lasers based on ZnO. The band gap of ZnO is tunable by alloying with e.g. Mg or Cd [2], leading way for blue and ultraviolet emission and thus denser optical data storage. If ZnO is doped with a magnetic element, such as Fe, Ni and Co, they dissolve in the ZnO crystal, making ZnO a so called dilute magnetic semiconductor(DMS). DMS devices may be used for spintronic applications – devices where both the charge and spin character of the electron is utilized for memory storage [3].

Hydrothermally grown ZnO provides relatively cheap high quality wafers,

which makes ZnO ideal for large scale production compared to its transparent counterpart indium tin oxide and its competing optoelectronic material gallium nitride.

The main obstacle for extensive use of ZnO in electronic applications is the remaining challenge of producing reliable p-type material and thus a pn-junction. Although p-type ZnO samples have been reported by several groups, the hole concentration and mobility are generally low. The low hole mobility reported is the main problem, because a reasonable majority carrier mobility is required in a working device.

The goal of this work was to investigate the correlation between carrier concentration and electron mobility in hydrothermally grown n-type ZnO samples as a function of post-growth heat treatment temperature. Hydrothermal ZnO typically contains significant amounts of residual impurity elements, amongst others lithium (Li). Li affects the substrate properties, as it acts as a compensating impurity in n-type ZnO, and thus reduces the charge carrier concentration. Further, as Li occurs frequently in an ionized state, it is a major contributor to ionized impurity scattering in ZnO.

Lithium is known to diffuse out of the bulk of the ZnO crystal at elevated temperatures [4–6]. To some extent, the objective of this work may therefore be rephrased to be an investigation of lithiums contribution to the electrical transport characteristics in hydrothermally grown ZnO. The methods used include temperature dependent Hall effect measurements (TDH), thermal admittance spectroscopy (TAS), secondary ion mass spectrometry (SIMS) and numerical calculations of the electron scattering processes related to the material quality, and their influence on the electron mobility.

Chapter 2

Background

In the beginning of this chapter some basic material and semiconductor physics will be summarized. This is only meant to clarify some important aspects that will be discussed later in the text. For a more thorough account of material science, refer to any standard textbook on the topic, such as references [7–10]. The second section covers the properties and synthesis of single mono-crystalline ZnO, as well as a review of some relevant previous work.

2.1 Basic material and semiconductor theory

2.1.1 Crystallography

A fundamental way of categorizing materials is by their structure; crystalline or non-crystalline. Non-crystalline materials are usually referred to as amorphous and are characterized by their lack of long range order in their atomic spatial arrangement. Glass is an example of an amorphous material. Its building block is the ${SiO_4}^{4-}$ tetrahedron, and each tetrahedron is linked to each other by shared corners. The difference between silica glass and crystalline quarts, which has the same ${SiO_4}^{4-}$ base unit, is illustrated in figure 2.1. The figure also shows the difference between crystalline and non-crystalline materials in general; they may consist of the same elements, but crystalline materials have a long ranging order.

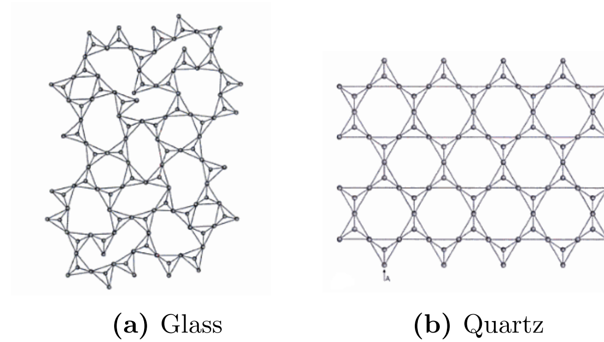

(a) Glass **(b)** Quartz

Figure 2.1 – The difference between amorphous and crystalline materials, exemplified by quartz glass and crystalline quartz. Both consists of the exact same $SiO_4{}^{4-}$ tetrahedron, but the glass lacks the long range order of a perfect crystal. From [10]

Crystals are usually described by their *Bravais lattice* and *basis*. The Braivais lattice describes equivalent points in space, i.e. the distances and angles between them, while the basis identifies the atoms in the material and their positions relative to the crystal points. Combined the Bravais lattice and the basis define the crystal structure unambiguously.

A unit cell is a volume that fills the entire space without any voids or overlapping when translated through a subset of Braivais vectors in the crystal lattice. They are practical for visual representations of the crystal structure, as they represent the smallest repeating unit in the crystal. The zinc oxide structure and unit cell will be discussed in the next section.

Miller indices are used to describe crystal planes and directions. A plane that intercepts the unit vectors of the structure at the points x, y and z is identified by the inverse of these coordinates; $\left\langle \frac{1}{x}\frac{1}{y}\frac{1}{z} \right\rangle$. For example, the $\langle 112 \rangle$-plane cuts the unit cell at $x = 1$, $y = 1$, $z = 1/2$ in units of the unit vectors. Negative indices are also allowed, and they are by convention written as $\bar{1}$ rather than -1. In the hexagonal crystal structure four indices are often used, $\langle h, k, i, l] \rangle$, where $i = -h - k$. This is not strictly necessary to define a plane, but it makes it easier to identify equivalent planes.

The hexagonal unit cell is defined by two basis vectors $\vec{a}$ and $\vec{b}$ of equal length with an angle of 60° between them defining a basal plane and a third vector $\vec{c}$ normal to this plane.

Defects and notation

A real crystal is never perfect – it contains defects. These defects may be 0-dimensional, such as vacancies or interstitials, 1-dimensional, such as dislocations, 2-dimensional, such as stacking faults, or 3-dimensional, such as precipitates. 1-, 2- and 3-dimensional defects are usually undesirable in active parts of electronic components, and can in principle be avoided with proper care during sample fabrication and processing. Native 0-dimensional defects, however, develop for thermodynamic reasons during fabrication. More defects contribute with more entropy in the material, and for that reason there is an equilibrium amount of defects in any sample, independent of the crystal growth method and cautions made during growth. Defects of this nature are called intrinsic, as they cannot be avoided and are not caused by impurities. The equilibrium amount of defects depends on the material, and hinges exponentially on temperature. It is however important to remember that real samples used for devices are rarely under defect equilibrium conditions. Examples of common defects in an elemental solid is given in figure 2.2.

Defects are written as the identity of the defect in normal letters, while the position of the defect in the crystal lattice is given in subscript. The charge of the defect is given by a superscript. A vacancy is denoted by V, and the interstitial position is denoted by I or i. For instance the donor defect "vacant oxygen position" is written V_O, while the acceptor defect "Li on Zn position" is written Li_{Zn}.

2.1.2 Semiconductors

Another approach to dividing materials into groups is based on their electrical properties. Using this approach materials can be divided into three main categories; metals, semiconductors and insulators, as illustrated in figure 2.3.

Vital to the understanding of this division is the concept of energy bands. The origin of distinct allowed electron energy states and the forbidden gaps between them is found in quantum physics. Two electrons can not occupy the same quantum mechanical state, and for that reason they occupy only discrete energy levels in atoms. In a continuous solid these allowed energy

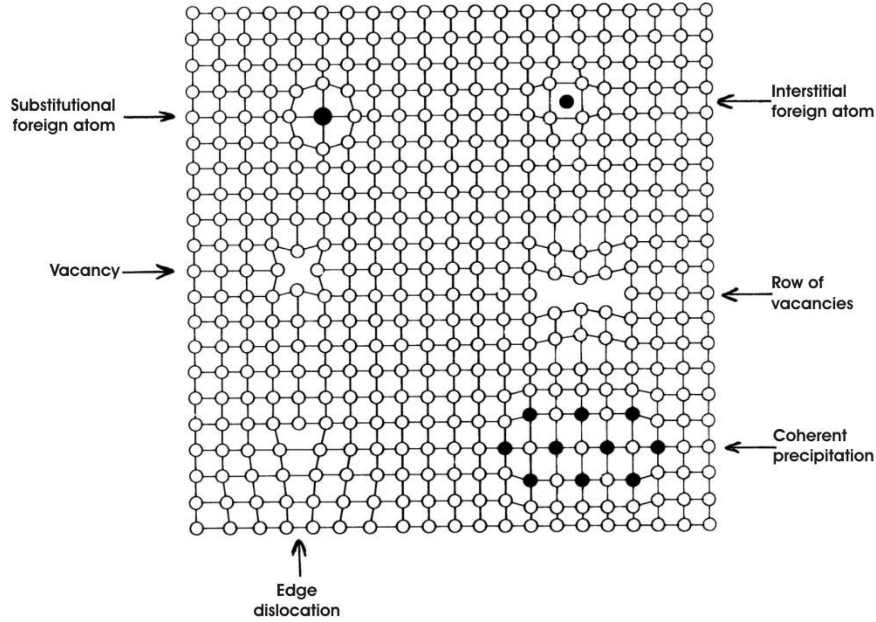

Figure 2.2 – Example of some defects in an elemental solid. Adapted from [11]

levels form essentially continuous bands [12], that may be separated by forbidden gaps. By forbidden gaps one means the lack of quantum mechanical energy states in the material the electrons can occupy. The difference in energy between two allowed bands in semiconductors and insulators is named the band gap, E_g. The chemist's approach to the band gap is more intuitively appealing as it is couched in real space. The band gap is the finite amount of energy required to take an electron from the bonding state to the antibonding state in a material, i.e. the transition from being localized as part of a bond between atoms to being delocalized and mobile in the material.

Another concept vital to the understanding of semiconductors is the Fermi level, E_f, named after the Italian physicist Enrico Fermi. The Fermi-Dirac distribution describes the probability for an electronic state with energy E in any system being occupied, and is given by

$$f(E) = \frac{1}{e^{(E-E_f)/kT} + 1} \tag{2.1}$$

In this equation k is Bolztman's constant and T is the absolute temperature.

The Fermi energy level in a material is defined as the level with a 0.5

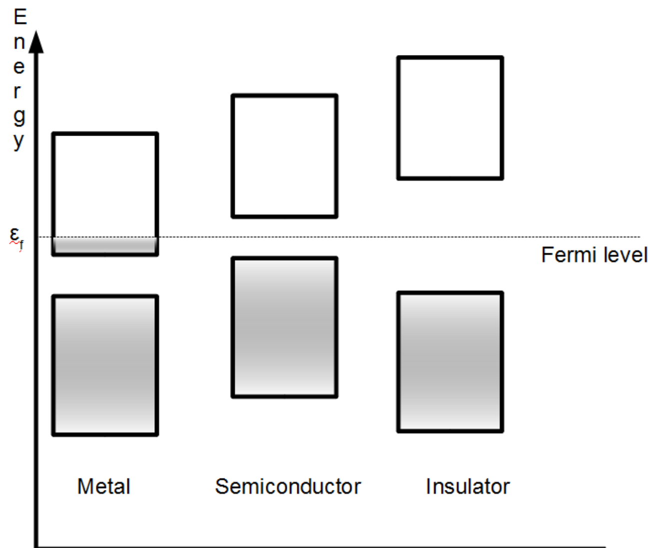

Figure 2.3 – The division of materials into metals, semiconductors and insulators based on the position and size of the band gap. The lower band is the valence band, and it is completely filled with electrons at 0 K. These electrons are tightly bound to the atoms in the crystal and contribute to the bonds between the atoms. The upper band is the conduction band, completely uninhabited at 0 K. Electrons in this band are delocalized, meaning that they are free to move and contribute to electric conduction under the influence of an electric field. There is no fundamental difference between an insulator and a semiconductor, but materials with a band gap of more than ∼3eV is often considered insulating rather than semiconducting. Intrinsic ZnO is thus a borderline material, but can easily be doped to achieve semiconducting behavior.

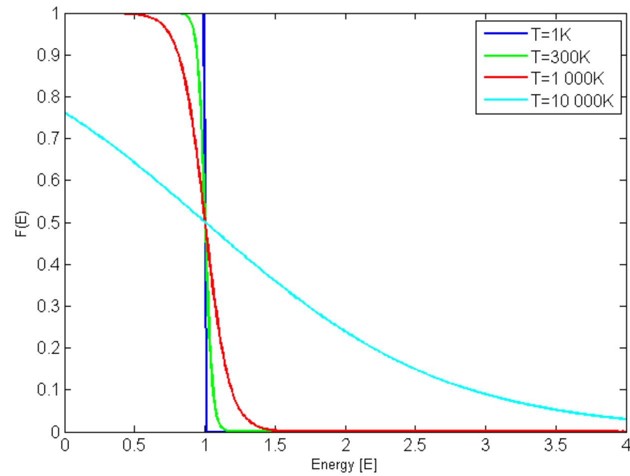

Figure 2.4 – Fermi-Dirac distribution as a function of energy at different temperatures. The energy is in units of Fermi energy.

probability of occupancy according to the Fermi-Dirac distribution. It is seen from equation 2.1 that at 0 K the Fermi distribution takes the shape of step-function. A state has either 1 or 0 probability for being occupied by an electron at this temperature. Put differently, the Fermi level is the highest energy level to be filled at 0 K. At higher temperatures, the distribution becomes more smeared out. This means that some energy levels with energy a few kT, where k is Boltzmann's constant, above the Fermi level may be occupied by electrons while some states below the Fermi level remain unoccupied. The Fermi-Dirac distribution at several temperatures is sketched in figure2.4.

If the Fermi level is located inside an allowed electron band, the electrons are free to move into any unoccupied state and electrical conduction can occur above 0 K. This is the case in metals. In semiconductors and insulators the Fermi level is located inside the forbidden band gap at 0 K. Every allowed electron state is thus occupied and the electrons are stuck in their valence state unless they by some mechanism are exited across the band gap into the conduction band. If the width of the band gap is in the range of a few kT the thermal energy is enough to excite some of them into the conduction band. This is known as electron-phonon interaction, where a phonon is a

quantum of thermal energy. Light, or photons, may also excite electrons across the band gap. In both cases the material becomes semiconducting. If the band gap is too large, electrical conduction is impossible at reasonable temperatures and the material is an insulator.

Electrons in the conduction band carry current in the obvious way. The *hole* (empty state) the exited electrons leave behind in the valence band is also a mobile and charged quasi particle, much the same as a vacancy in the crystal. Holes, denoted h^+, have the same elementary charge as electrons, but with opposite sign as they are positively charged.

Band structure

The band diagrams in figure 2.3 are simplified because they do not include any variable at the horizontal axis. A more correct, but still strongly simplified representation is shown in figure 2.5. On the y-axis is the energy as before, while the variable on the x-axis is the *k-vector*. The origin of the k-vector is the quantum mechanical wave representation of the electron. $\vec{k}$ is named the wave vector with units m^{-1}, and it is related to the electrons momentum through the relation $\vec{p} = \hbar\vec{k}$, where $\hbar$ is Planck's constant. The difference between the semiconductors in figure 2.5 is that in the example on the left hand side the valence band energy maximum is at the same $\vec{k}$-value as the conduction band energy minimum. In the picture on the right hand side the situation has changed, and the maximum and minimum positions are shifted with respect to $\vec{k}$. This illustrates the difference between a direct and an indirect semiconductor. *In a direct semiconductor an electron transition between the bands can occur without a change in electron momentum.* When a conducting electron recombines with a hole in the valence band in a direct semiconductor, a photon with energy equal to the band gap energy is emitted. In an indirect material this transition is much less likely to occur, because an electron-phonon interaction is required to change the electrons momentum. As this mechanism involves interaction between the electron and the lattice atoms, primarily heat is produced rather than light. Only direct semiconductors can be used with high efficiency for certain optical applications, such as LEDs.

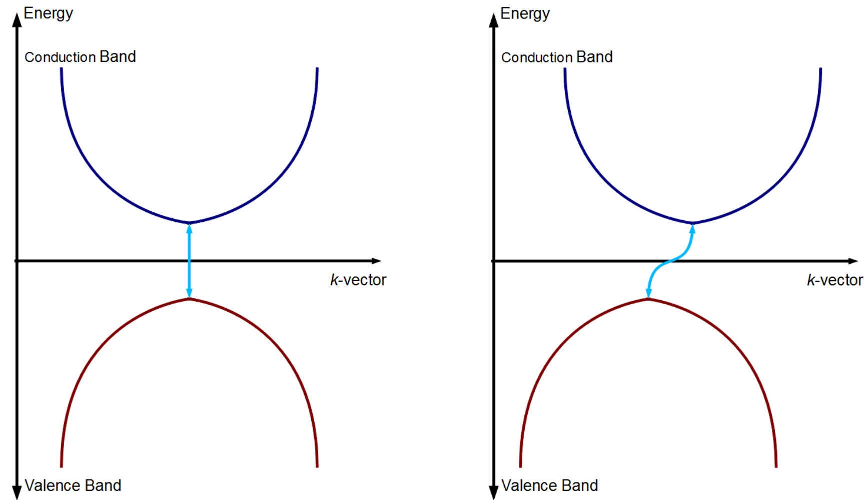

Figure 2.5 – Schematical drawing of a direct (left) and an indirect (right) band gap. For a recombination of a electron and hole in an indirect semiconductor to occur, a phonon interaction is needed. This transition is thus less probable, and the energy equal to the difference between the two states is readily transfered to the lattice as vibrational energy (heat).

Defects in semiconductors

A perfect semiconductor without impurities is called intrinsic, as opposed to an extrinsic semiconductor which contains impurities. Intentional impurities is referred to as doping, and proper doping is the key to producing working devices. Dopants are incorporated into the crystal lattice, usually at substitutional positions, and the doping concentration is given in the units of cm^{-3}. For reference, the concentration of the native atoms in a semiconductor, e.g. the amount of Si atoms in silicon, is usually in the $10^{22} cm^{-3}$ range [13]. Dopants have a higher or lower valency than the element they are substituting. The role of the dopant is to act as donors or acceptors, i.e. increasing the electron or hole concentration in the material, by being ionized in the lattice.

In the band diagram, doping gives rise to additional states within the band gap, to and from which electrons can be excited. This allows extrinsic semiconductors to conduct current several orders of magnitude better than

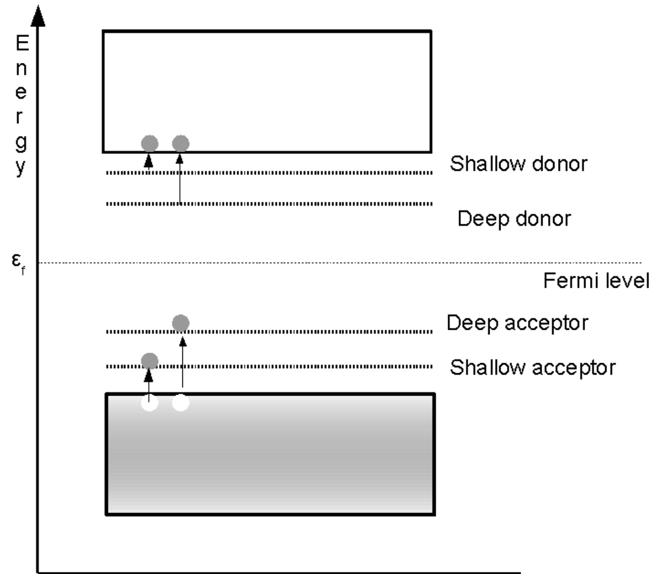

Figure 2.6 – Doping introduces new levels within the band gap.

their intrinsic counterparts. Acceptor doping gives *p-type* material, i.e. the conduction is dominated by holes, while donor doping gives *n-type* material. Other defects, including the intrinsic ones, also give levels in the band gap. V_O, for instance, gives a donor level near the conduction band edge in ZnO.

The acceptor and donor levels are defined as shallow or deep depending on their position relative to the band edge. Deep defects may act as either trapping or recombination centers, depending on the impurity, temperature and other doping conditions. [14] Shallow centers have a low excitation energy, around 0.01-0.10 eV from the band edge. [15] Unless the concentrations of the donor and acceptor impurities are very small, they will be a far more important source of carriers than the intrinsic mechanism of exciting carriers across the full band gap. This is especially important for wide band gap materials.

Electrical conduction in semiconductors

In a semiconductor both holes and electrons contribute to the current. The drift current density is given by

$$J_x = q(n\mu_n + p\mu_p)\mathcal{E}_x \tag{2.2}$$

where q is the elementary charge, n and p are the electron and hole concentration respectively and $\mathcal{E}$ is the electrical field causing the current. As the carrier concentration follows the law of mass action, i.e. $n \times p = constant$, it can be seen that one carrier type will dominate the conduction in an extrinsic material. μ in the equation refers to the *mobility* of the carrier. The mobility of the carriers describe the ease with which the carriers drift in the material, and can be compared to friction or drag in classical mechanics. The carrier mobility is a very important property of a semiconductor. It is defined for electrons as

$$\mu_n \equiv \frac{e\tau_n^{coll}}{m_n^*} \tag{2.3}$$

and in a similar way for holes. In the equation τ_n^{coll} is the average time between scattering events, while m_n^* is the effective mass of the conduction electrons. Another, and more intuitive, expression for the mobility is

$$\mu_n = -\frac{\bar{v}_x}{\mathcal{E}_x} \tag{2.4}$$

Here $\bar{v}$ is the average drift velocity of the electron, and the mobility is thus the drift velocity maintained by the electron per unit electric field. For holes the same expression is valid, only without the negative sign since they move in the same direction as the field. Mobility is usually expressed in the unit $[\frac{cm/s}{V/cm} = cm^2/Vs]$.

It is assumed that different scattering events occur independent of each other if they are caused by different mechanisms. This concept is known as Matthiessen's rule [15,16]. In the relaxation time approximation this implies that the total relaxation time is the reciprocal sum of relaxation times for each event.

$$\frac{1}{\tau_{tot}} = \frac{1}{\tau_1} + \frac{1}{\tau_2} + \cdots \Longleftrightarrow \frac{1}{\mu_{tot}} = \frac{1}{\mu_1} + \frac{1}{\mu_2} + \cdots \tag{2.5}$$

The subscripts represent different scattering mechanisms. This means that the scattering mechanism causing the lowest mobility is the dominant one. This will be clearly illustrated later, when Hall data are evaluated.

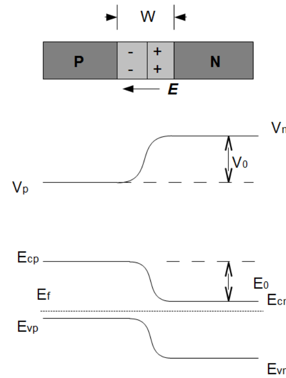

Figure 2.7 – The pn-junction. Top: Actual junction with ionized impurities in the depletion region. Intermediate: The built in potential across the junction, caused by the ionized impurities Bottom: The separation of the energy bands. The Fermi level is unchanged throughout the junction.

2.1.3 Junctions and contacts in semiconductors

In this section some of the physics of semiconductor junctions and contacts to semiconductors are summarized. Again, the reader is referred to any standard textbook on the topic, e.g. [15] for further in-depth details.

pn-junctions

If p- and n-type semiconductors are brought to intimate contact, a junction is formed. Because of the doping, the Fermi level is above and below mid band gap for n- and p-type material respectively. It is however a criterion for materials in equilibrium that the Fermi level remains constant throughout the whole sample, so that $dE_f/dx = 0$. To fulfill this criterion, the majority carriers will diffuse across the junction, leaving the ionized dopants uncompensated. This will give rise to a difference in potential across the junction (V_0) and a so called *space charge region* on both sides of the junction will result. Any mobile charges in the space charge region will be swept across the junction by the built in electric field. This region is thus depleted of free charge carriers and is often referred to as the *depletion region*. Here, the depletion region width is referred to as W. The situation is summarized in figure 2.7.

One of the main features of a pn-junction, or pn-diode as this device is named, is its rectifying behavior. This is because an external bias will increase or decrease the potential step the charge carriers experience upon crossing the junction.

The width of the depletion region is given by the charge balance requirement combined with *Poission's equation*. If the space charge region reaches from the metallurgical junction and a length x_{n0} and x_{p0} into the n and p side respectively, the following equation must be fulfilled

$$qAx_{p0}(N_a^- + p) = qAx_{n0}(N_d^+ + n)$$

where N_a and N_d are the acceptor and donor doping concentration respectively. If it is assumed that the depletion region is indeed completely depleted of free charge carriers, and that the device's cross-section is unchanged through the junction, this simplifies to

$$x_{p0}N_a = x_{n0}N_d \tag{2.6}$$

The Poisson equation states that the change in electric field is given by

$$\frac{d\mathcal{E}}{dx} = \frac{q}{\epsilon}(p - n + N_d^+ - N_a^-) \tag{2.7}$$

With these assumptions and some algebra found in reference [15], the following result is achieved:

$$V_0 = \frac{1}{2}\mathcal{E}_0 W = \frac{1}{2}\frac{q}{\epsilon}N_d x_{n0} W = \frac{1}{2}\frac{q}{\epsilon}N_a x_{p0} W \tag{2.8}$$

Here $\mathcal{E}_0$ is the maximum value of the electrical field in the junction. Keeping in mind that W is just $x_{p0} + x_{n0}$, so that $x_{n0} = WN_a/(N_a + N_d)$, one gets

$$V_0 = \frac{1}{2}\frac{q}{\epsilon}\frac{N_a N_d}{N_a + N_d}W^2$$

or, solved for W

$$W = \left[\frac{2\epsilon V_0}{q}\left(\frac{N_a + N_d}{N_a N_d}\right)\right]^{1/2} = \left[\frac{2\epsilon V_0}{q}\left(\frac{1}{N_a} + \frac{1}{N_d}\right)\right]^{1/2} \tag{2.9}$$

From this it is clear that in a diode where one side of the junction is more heavily doped than the other, the depletion region reach mainly into the lightly doped side of the metallurgical junction.

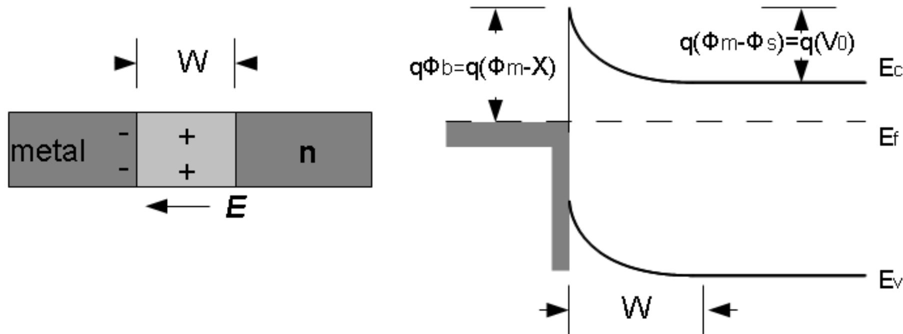

Figure 2.8 – Left: The metal semiconductor interface. Right: The band diagram of the same junction.

Schottky barriers

A similar situation as the one in the pn-junction may arise in a metal semiconductor junction, depending on the *work function* of the metal as compared to the semiconductor.

The work function of a material, $q\Phi$, is defined as the difference in energy between the Fermi level and the vacuum level, i.e. the (hypothetic) level where the electron has no interaction with the material it originates from or any other electrons. This is a useful value, because it makes it possible to evaluate the position of Fermi levels in two materials compared to each other. A metal-semiconductor contact where the metal's work function is larger than the semiconductor's will be used as an example.

In order to align the Fermi levels of the metal and semiconductor, charge flows from the semiconductor into the metal, creating a potential barrier, V_0, which prevents further charge diffusion. As in the pn-diode, an external bias will increase or decrease the barrier height. The depletion region reaches primarily into the semiconductor, as the metal compensate the charge on the surface only. See figure 2.8 for details.

When doing junction spectroscopic experiments on ZnO, such as thermal admittance spectroscopy or deep level transient spectroscopy, Schottky bar-

riers are needed. When the capacitance of a semiconductor-metal contact is evaluated, the standard parallel-plate capacitor model is used with the depletion region acting as the dielectric between the plates, and W the separation distance between them.

Ohmic contacts

Ohmic contacts have a linear current-voltage relation, and are crucial for many applications. They can be formed in two ways:

1. The work function of the metal is smaller than the semiconductors for n-type, and the opposite for p-type.
2. The semiconductor is heavily doped, giving a steep potential barrier and narrow depletion region, through which tunneling of the charge carriers can occur.

Ohmic contacts are extensively used in this study for the TDH measurements.

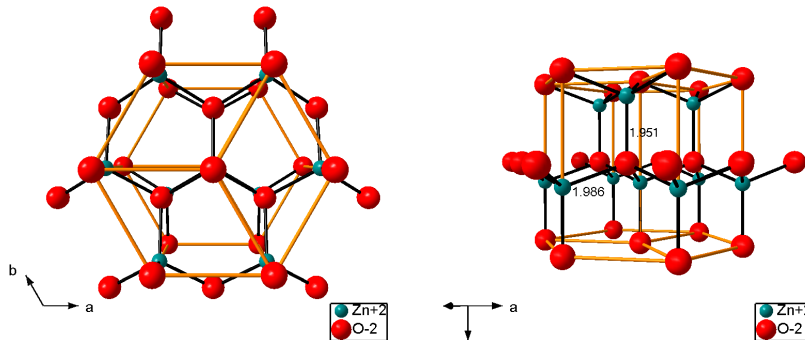

Figure 2.9 – The zinc oxide wurtzite structure viewed along and perpendicular to the z-axis respectively.

2.2 Zinc oxide

2.2.1 Structural properties of zinc oxide

Zinc oxide crystallizes in the wurtzite structure under normal conditions, and the structure is shown in figure 2.9. This structure is hexagonally close packed with cell parameters a=b=3.25Å and c=5.21Å [17, 18]. The ratio c/a=1.60 between the $\vec{a}$ and $\vec{c}$ unit vectors is close to the ideal close-packed value. The structure belongs to the space group $P6_3mc$, which is a term mostly used in mineralogy [10]. In the wurtzite structure, all the octahedral and half of the tetrahedral sites are vacant, and it is therefore no surprise that interstitials are among the dominant point defects in ZnO. [19] The oxygen atoms lie within an imperfect tetrahedron; the Zn-O bond along the c-axis is shorter than the other three. This gives rise to the piezo-, pyro-, ferro-, and dielectric properties of ZnO. The $\langle 000\bar{1} \rangle$-face is usually referred to as the O-face as it is oxygen terminated, while the opposite $\langle 0001 \rangle$-face is zinc terminated. The polarity of the material affects i.a. the diffusion of some dopants.

2.2.2 Synthesis of single crystal ZnO

High quality bulk zinc oxide can be produced by different methods. Some of them will briefly be mentioned here, mostly based on the summary in

reference [20].

Gas-transport technique

In this method purified ZnO powder is reduced to Zn vapor by carbon or hydrogen at elevated temperatures. The vapor is transported to a colder area in the growth chamber where it reacts with oxygen gas. This gives high quality single crystal needles of high purity.

In the seeded growth method, the Zn vapor is transported by a carrier gas, e.g. H_2, to a single crystal ZnO seed. State of the art seeded growth samples can reach diameters of 2 inches of very good quality, and the growth rate can be higher than 1mm per day.

Hydrothermal growth

With the hydrothermal method, ZnO is dissolved in a KOH/LiOH base solution at elevated temperatures (300 - 400 °C) and pressure (70 - 150MPa). ZnO is grown from the solution by seeded growth, in a part of the autoclave which has lower temperature. Most of the impurities from the base material are lost during the process. However, lithium or potassium contamination is usually present in hydrothermally grown samples, depending on which solvent is used. Their concentration may be as high as the $10^{17} - 10^{18} cm^{-3}$ range. Some of the advantages of the method are the relatively low temperatures involved, the superior throughput and manufacturing cost, and the scalability. Another important advantages is the possibility for *in situ* doping [21]. One of the disadvantages of hydrothermal synthesis is the low growth rate of 0.06-0.25 mm per day.

Melt growth

The fastest method for ZnO growth is from a melt. Cermet Inc has patented a method where an oscillating electric field is used to melt ZnO by induction under O_2 overpressure in a cold-wall crucible. In this way, contamination from the container is limited and reduction to non-stoichiometric $Zn_{1-x}O$ is avoided. The diameter of the samples is usually ∼1 cm and the growth rate is as high as 1-10 mm per hour. If a clean source of ZnO is used, excellent

quality samples can be made. The method is scalable and thus interesting for comercial production [22].

Common for all the above mentioned growth methods is that they produce unintentional n-type material. The reason for this n-type behavior will be discussed in the next section. ZnO can also be grown in epitaxial layers by several methods including Metal-Organic Chemical Vapor Deposition (MOCVD), Molecular Beam Epitaxy (MBE) and sputtering.

2.2.3 Defects and doping of ZnO

Intrinsic donors

Zinc oxide without any intentional doping always shows n-type behavior. Although zinc oxide has been studied for many years there is little consensus in the literature on which intrinsic donor being the dominant one.

The oxygen vacancy, V_O, is a well know donor in most functional oxides, and it is also present in ZnO. In oxygen deficient conditions V_O is considered to be the dominating donor in metal oxides, according to general defect chemistry [11]. One would expect this to be the case in ZnO as well, and V_O is shown to be the native defect with the lowest formation energy under Zn-rich conditions. Still, the formation energy of V_O is high, giving only low concentrations, even at high growth temperatures [20]. In addition extensive calculations based on density functional theory (DFT) done by Janotti and van der Walle [23] shows that the oxygen vacancy is a deep donor, leaving it neutral at room temperature. This makes V_O an unlikely candidate for being the dominant donor in ZnO. However, according to the same authors the oxygen vacancy may be an important recombination center, preventing conversion to p-type material.

The zinc interstitial is another intrinsic donor. Zn_i gives a shallow donor level [20], but it does also have a high formation energy according to Jannoti and van der Walles calculations. This makes it, according to these authors, an unlikely candidate to cause n-type conduction, because it will be present

only in very low concentration. D C Look et al. however, conclude in one article that the dominant residual defect in ZnO is the zinc interstitial [24].

A third intrinsic donor in ZnO is the zinc anti site Zn_O. It has a low donor ionization energy, but a high formation energy, and is thus not likely to cause n-type conduction.

Extrinsic donors

Since it seems clear from the discussion above that the predominant n-type behavior of ZnO is not likely to be caused by any native impurity alone, it is natural to consider residual donor impurities. Many impurities introduced during growth or processing may contribute to zinc oxide's n-type behavior. In principle any group III metal on a zinc position will act as a donor, and many of them have been tried with success [25]. In addition, the introduction of a group VII element, such as fluorine, on an oxygen position will make the material n-type.

In most semiconductors hydrogen is amphoteric, meaning that it can be present as a donor, either a proton, H^+, or a OH^+-group, as the neutral atom, H_i or as the electron acceptor H^- ion. ZnO is special because hydrogen appears exclusively in the H^+ state, i.e. acting as a donor [20, 26]. Experimentally, hydrogen has been known to act as a donor since the 1950s when Mollwo did his pioneering work on hydrogen in ZnO. He observed an increase in conductivity as the ZnO samples was heated in H_2 atmosphere. When the hydrogen ambient was removed, the conductivity recovered to its original value [27]. Later Thomas and Lander [28] did a similar experiment, but they also included the H_2 partial pressure as a variable. They suggested the increase in conductivity to originate from an O-H^+-group or a H^+ interstitial. Hydrogens role as a donor was confirmed by Hutson [29], and its ionization energy was measured to be $\sim$50meV by the same author. van der Walle did a famous first priciple DFT calculation on hydrogen in ZnO in 2000, suggesting that hydrogen was *the* cause of zinc oxides n-type behavior [26]. However, ZnO is still a n-type material after high temperature anneals, at which hydrogen diffuses out of the sample, indicating that at least one more intrinsic or impurity donor is causing ZnO to be n-type.

Aluminum or other group III are suggested to be likely impurities causing ZnO to be n-type, and indeed Al is used extensively for n-type doping. It is nevertheless unlikely that Al or other metal impurities are present in such high quantities in every growth method available.

In summary, the reason for the inherent n-type behavior of ZnO is still a question open for debate, and no full consensus has been reached in the literature.

Acceptors

In order to make many useful ZnO devices, such as light emitting diodes or lasers, p-type material is needed. Despite countless efforts to acceptor dope ZnO, it has proved quite a challenge to make lasting and reproducible p-type samples. The intrinsic acceptors in ZnO are V_{Zn} and O_i. The zinc vacancy have been studied by positron annihilation spectroscopy, and has been proved to be the dominant intrinsic acceptor in n-type material [30].

At a first glance, p-doping of ZnO does not seem that hard to accomplish, if for instance alkali metals (group I elements) such as lithium, sodium or potassium are substituted for Zn in the crystal structure. Since these elements have one less valence electron than Zn, they are compensated by one hole in the valence band when ionized. Another approach is to substitute oxygen with a group V element such as nitrogen, phosphorus, arsenic or antimony (Sb). Group IB metal doping, for instance by copper, can also be used to make p-type ZnO [31]. However several problems arise when synthesizing p-type ZnO:

1. Low dopant solubility.
2. The dopant energy level is not sufficiently shallow.
3. The dopant is compensated by native defects or residual impurities.
4. The dopant shows amphoteric behavior, i.e. it acts as a substitutional acceptor but also as a interstitial donor.

Despite the problems mentioned above, p-type ZnO has been reported with Li-, As-, Sb- P- [2] and N-doping [32]. It has even been reported p-type

ZnO grown by Single Source Chemical Vapor Deposition (SSCVD) in controlled oxygen rich atmosphere. In this case the p-type behavior is believed to be caused by Zn vacancies, reducing the substantial problem of unintentional donor compensation [33]. Growing homo epitaxial layers on top of n-type wafers by this method, possibly combined with other dopants, may be a route to the realization of ZnO pn-junctions.

The understanding of lithiums role in ZnO is important, both because it is a possible candidate for p-type doping, and also because it is a common compensating impurity in as-grown hydrothermal samples. Lithium is amphoteric in zinc oxide; it can appear as both Li_{Zn} and Li_i, causing high resistivity material with low carrier concentration and low electron mobility. A pioneering study on lithium in zinc oxide was done by Lander in 1960 [34] while investigating lithium's role as a possible p-type dopant. It was found that lithium diffuses fast into the sample as Li_i, but at elevated temperatures it is incorporated into the crystal as Li_{Zn} and acts a compensating impurity, confirming lithiums amphoteric behavior.

Later it has been calculated that the interstitial configuration of Li is more stable than the substitutional one in p-type material [35], making p-type ZnO based on Li substitution hard. Other calculations show that hydrogen passivated Li_{Zn} is more stable than Li_i so that an annealing step may possibly activate Li_{Zn} acceptors as H leaves the sample at high temperatures, [36] and Li-doped p-type material has been reported in the literature [37].

In n-type material, Li_{Zn} is much more abundant than Li_i, and Li is thus considered to act exclusively as an acceptor [6].

2.3 Previous work

Zinc oxide is a hot topic in the international semiconductor research community. Some previous work which is relevant to the topic of this thesis is presented below, but a complete review is not attempted. Ü. Özgür et al. has written a comprehensive review on almost every aspect of ZnO [2], while Monakhov et al. [21] has written an award winning review on growth, the role of hydrogen and Schottky diodes to ZnO, if further background knowledge is needed.

Systematic studies of the lithium concentration as a function of post-growth annealing temperature was done by Maqsood et al. [4]. Hydrothermally grown ZnO wafers were isochronally heat treated (1 hour) in the temperature range 600 °C - 1600 °C. The lithium concentration was measured with (SIMS) and the carrier concentration was estimated from the result of four point resistivity measurements. Up to temperatures around 1000 °C, the lithium concentration seemed to remain unchanged at around 1-2 $\times$ 10^{17}cm^{-3}. In the range 1000-1200 °C the bulk lithium concentration decreased, eventually falling bellow the SIMS detection limit (about 3$\times$ 10^{13}cm^{-3}) at around 1500-1600 °C . Another important result was that Li get caught by trapping centers near the sample surface, increasing the Li concentration near the surface by several orders of magnitude compared to the as-grown sample. The main results are summarized in figure 2.10. Maqsood's work is in many respects similar to the work presented in this thesis, the annealing is done in a similar way on the same kind of samples, but instead of resistivity measurements, the carrier concentrations are estimated from TDH measurements.

Schifano et.al. has done an investigation on as-grown hydrothermal ZnO wafers with TDH measurements, TAS and SIMS as the main experimental tools [38, 39]. The energy level positions and concentrations of three donors and the concentration of one compensating acceptor was determined. The results are summarized in table 2.1. The samples investigated showed a carrier concentrations in the $10^{15} - 2 \times 10^{16} cm^{-3}$ range at room temperature for the three samples, and a peak electron mobility of $\sim$ $125 cm^2/Vs$ at $\sim 200K$. All samples were highly compensated as shown in table 2.1.

The E_3 donor level ($E_C - 0.3eV$, named after reference [40]) reported by Schifano et al. [38, 39] is frequently reported in literature, and appears in most zinc oxide samples, regardless of growth method [21]. It is thus believed to be of intrinsic nature, and V_O was first suggested. However, other intrinsic or extrinsic donors or impurity complexes have also been suggested. Indeed, the E_3 level is reported by some authors to consist of two distinct energy levels E_3 and E_3', whose positions in the band gap are very close to each other [41].

The E_2 donor level positioned at $E_C - 50meV$ is believed to be caused by

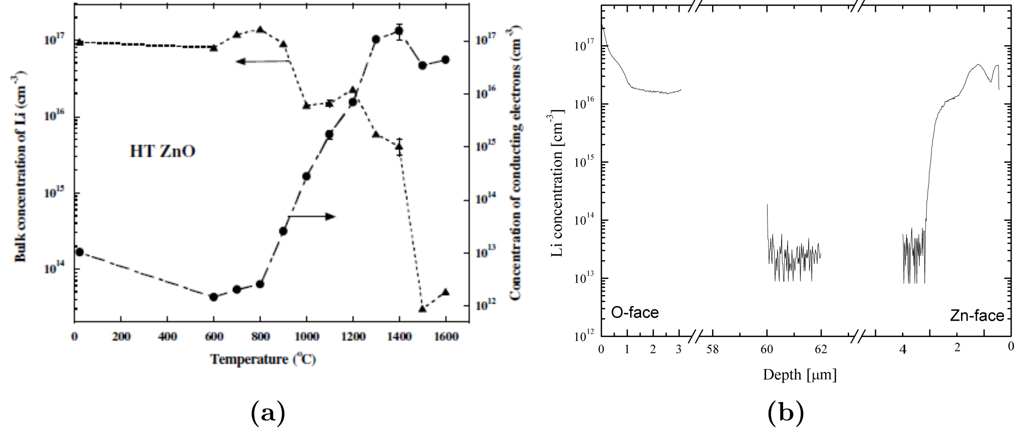

(a) (b)

Figure 2.10 – (a): The resistivity and estimated carrier concentration as a function of annealing temperature. A mobility of $210cm^2/Vs$ is assumed for the carrier density estimation. It will be shown later that this mobility value is to high for hydrothermal samples, and also that it varies as a result of the heat treatment. This makes the estimations presented here for the carrier concentration too low by approximately a factor 2. (b): The Li concentration as measured by SIMS. Notice the large difference in Li concentration in the bulk and at the sample surface. From [4]

N_{D1},	E_{D1}	N_{D2}	E_{D2}	N_{D3}	E_{D3}	N_a
2.0 ± 0.4	30 ± 10	1.3 ± 0.1	50 ± 10	$3 - 7$	300 ± 40	3.1 ± 0.4
1.5 ± 0.4	30 ± 10	1.5 ± 0.1	50 ± 10	$0.4 - 7$	290 ± 30	2.9 ± 0.4
0.8 ± 0.4	30 ± 10	1.3 ± 0.1	50 ± 10	1.1 ± 0.3	290 ± 40	2.3 ± 0.4

Table 2.1 – The concentrations and energy positions of three donors and the acceptor concentration found by Schifano et al. [38, 39] in three hydrothermal samples similar to those used in this work. A combination of TDH and TAS measurements was used to determine the variables. All concentrations are given in $10^{17}cm^{-3}$ and all energies in meV.

av extrinsic donor. The concentration of the E_2-donor determined by THD measurements fits well with the aluminum concentration found by SIMS in Ref. [39], and also other papers report this level to be the Al_{Zn} (or also possibly Ga_{Zn}) donor [42].

The E_1 level was observed by Look et al. [42], and it was believed to be related to intrinsic defects, as its concentration increases after 1MeV electron radiation. They attribute the E_1-level to interstitial zinc, or more precisely the related and more stable (Zn_i-N_O)-complex, and also suggests that this is the dominant intrinsic donor in ZnO grown by the vapor phase method.

von Wenkstern et al. [41] report a very shallow donor in hydrothermal ZnO located only 12meV bellow the conduction band, which was named T_1. This defect was found in samples annealed at above 600 °C, but no suggestion was made with regards to the origin of this level. They also observed the E_3 and E_2 levels, and a fourth level situated at $E_c - 47meV$, which they attributed to hydrogen. This means that within the experimental and fitting errors of the Hall effect technique, the H and Al levels may be hard to separate.

Deep level transient spectroscopy (DLTS) (see reference [43] for a good introduction to the method) and SIMS was employed by Vines et al. [5] to investigate deep levels in hydrothermal ZnO after a sequence of high temperature post growth anneals in the interval between 1100 °C and 1500 °C. The aim of the study was to find a correlation between the concentration of electron traps in the upper part of the band gap and the concentration of the most prominent impurities. The investigation confirmed that the E_3 defect is not related to Li, and in fact the concentration of the defect was shown to decrease after anneals in the 1250 - 1500 °C interval. Further it was shown that Li was the only one of the prominent impurities (Al, Mg, Si, Fe, Mn and Ni) to change its concentration as a result of the anneal. Two more donor levels were identified, at $E_C - 0.19 \pm 0.03eV$ and $E_C - 0.58 \pm 0.03eV$. The $E_C - 0.19eV$-level may be related to Li, but this was not definitely confirmed. The $E_V - 0.58$-level was only found in selected samples, any may therefore be impurity related, but no correlation with the main impurities detected by SIMS was reported.

In a study performed by Auret et al. [40], a combination of DLTS and

TDH was done. The most prominent defect found in this study was a defect located at $E_C - 0.120eV$, later referred to as L_2. This level was observed by DLTS, but not by TDH measurements. In stead two shallows levels at $E_C - 0.61meV$ and $E_C - 0.31meV$ was detected by the Hall measurements. It was speculated that the level at 120meV found by DLTS and the level at $E_C - 61meV$ may actually be the same level, with a temperature activated capture cross section, with a energy barrier of 59meV.

Finally, Yang et al. [44] have investigated ZnO grown by different methods applying TDH measurements as the main analysis tool. The samples were grown by high-pressure melt (HP), seeded chemical vapor transport (CVT) and by hydrothermal (HT) methods. The hydrothermal sample was dominated by extrinsic scattering over the whole temperature range, while the two others behaved nearly intrinsic. Of the three samples, the hydrothermal one had the lowest carrier concentration ($n_H = 2.5 \times 10^{14} cm^{-3}$, three order of magnitude lower than the others) and the lowest electron mobility ($\mu_H = 134 cm^2/Vs$, compared to $\mu_H = 203 - 205 cm^2/Vs$ for the other two) at room temperature. The hydrothermal sample also showed a very rapid decrease in mobility at low temperatures, indicating electron 'hopping' conduction between donors instead of the conventional band conduction. The article also presents a very interesting prediction on the maximum possible mobility for electrons and holes in ZnO. The values stated are $\mu_H = 220 - 230 cm^2/Vs$ at room temperature (RT) and $\mu_H = 2850 cm^2/Vs$ at 60K. For holes the intrinsic value is $\mu_H = 69 cm^2/Vs$ at RT. Reports of hole mobility significantly higher than this may thus indicate nonuniform samples.

Chapter 3

Experimental methods

This chapter introduces the experimental methods used during the characterization. Please refer to the given references for further in depth details and explanations.

3.1 Annealing

Thermal annealing [19] is a process where the sample is heated for a predetermined duration and temperature. The purpose of the anneal is to activate certain temperature dependent processes, such as electrical activation of dopants, diffusion or relaxation of distorted crystals. Sometimes compromises have to be made with regards to temperature and time, for instance when one wants to reduce implantation induced damage in a sample by annealing, and simultaneously wants to avoid the implantation profile from being broadened by diffusion. In order to avoid diffusion, annealing time can be reduced to just a few millisecond by using different rapid thermal annealing (RTA) methods, e.g. flash annealing. The third parameter is the annealing atmosphere. Typically air or inert gases are used, but other gases, like O_2, may also be used in order to manipulate the sample stoichiometry.

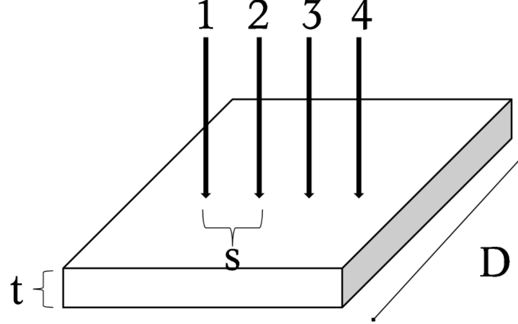

Figure 3.1 – Schematic representation of a four-point resistivity measurement.

3.2 Four-point resistivity measurements

To get an accurate measure of the resistivity of semiconductor samples, the four point probe measurement is employed. It has the advantage over the simpler two point measurement that the resistance of the wiring and contacts can be neglected, and is more accurate for low resistance samples and samples with high contact resistances. During measurements, current is passed through the sample from probe 1 to 4, and the potential drop between probe 2 and 3 is monitored, see fig3.1. The resistivity of the sample is given by [43]

$$\rho = 2\pi s F \frac{V}{I} \tag{3.1}$$

where s is the probe spacing, F is a geometric correction factor, V is the measured voltage and I is the current. For a semi-infinite sample F approaches unity, but for any sample of modest dimensions F needs to be taken into account. For collinear probes with equal spacing, F can be written as the product of three separate correction factors

$$F = F_1 F_2 F_3 \tag{3.2}$$

In the case of a semiconductor sample on a non-conducting bottom sur-

face, F_1 is given by

$$F_1 = \frac{t/s}{2\ln\{[\sinh(t/s)]/[\sinh(t/2s)]\}} \tag{3.3}$$

where t is the sample thickness. This factor corrects for the sample's finite thickness. F_2 corrects for the lateral dimensions of the sample, and is given by

$$F_2 = \frac{\ln 2}{\ln 2 + \ln\{[(D/s)^2 + 3]/[(D/s)^2 - 3]\}} \tag{3.4}$$

The equation applies to circular samples with diameter D. In the case of square samples, the same correction is valid as long as $D/s > 15$, with D being the length of the sample side instead of it's diameter.

F_3 corrects for edge effects, and is in most cases assumed to be unity. This is correct if the probe is placed at least 3-4 probe spacings from the sample edge.

If the mobility of the charge carriers in the material is known, and the contacts to the material are Ohmic, resistivity measurements can give an estimate of the majority carrier concentration through the relation given by equation 2.2 [15].

$$\frac{1}{\rho} = q(n\mu_n + p\mu_p) \tag{3.5}$$

The sample has to be dominated by one carrier type only in order to solve the equation for carrier concentration. As described in the previous chapter, μ is shown to be strongly dependent on growth method for ZnO samples.

3.3 Secondary Ion Mass Spectrometry

Secondary Ion Mass Spectrometry (SIMS) is en extremely powerful method for analyzing the amount of impurities in solid materials [4, 45, 46].

SIMS is based on sputtering of atoms from the surface of the sample under test. A beam of ions is focused at a point on the sample surface, usually O_2^+ or Cs^+. These ions are referred to as primary ions, and their energies are typically in the 3-15keV range. As the primary ions transfer their momentum to the sample, some fragments are sputtered off the surface. These fragments include atoms, ions and some neutral or ionized clusters of

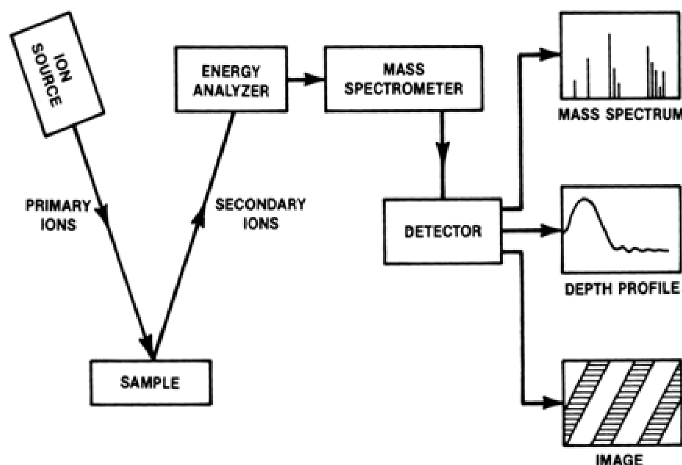

Figure 3.2 – A principal sketch of the SIMS' mode of operation.

atoms. Only the sputtered ions, from now on referred to as the secondary ions, are used for further analysis. First, the secondary ions are separated by an energy analyzer. This is done by passing them through a electric field which bends the secondary beam before passing through a slit. The isoenergetic ions are then passed through a magnetic field where they are separated by momentum. The remaining secondary ions are detected, and they all have the same *mass-to-charge* ratio:

$$\frac{M}{q} = \frac{r_m B^2}{r_e E_0} \tag{3.6}$$

where r_e and r_m are the radii of the ions trajectory in the electric and magnetic field separators respectively, B is the magnetic field strength and E_0 is the electrical field strength. By changing the magnetic field strength, the mass-to-charge ratio is changed accordingly.

The detectors used for the SIMS analysis records only the number of counts per unit time as a function of magnetic field in the momentum selector. Hence, a good calibration is needed since the intensity measured for each species is dependent on factors such as the erosion rate, sputtering yield and ionization probability etc, where the latter one is difficult to estimate accurately. Under optimum conditions, impurity concentrations lower than

one part per billion can be detected by SIMS. In mass spectrometry mode, the whole spectrum of mass-to-charge ratios is measured, and a bar graph of the different species' relative occurrence is acquired.

The counts per time values from the detector can be translated into concentrations per depth values if the sputtered crater depth is determined. This makes SIMS suitable for measuring doping profiles and layered structures. Imaging is also a possible operation mode. The image is a "map" of the composition of the sample, which is very useful for instance for failure analysis in integrated circuits.

Unique for SIMS is the large dynamic detection range, more than five orders of magnitude. The depth resolution is excellent, and can reach values as low as 2 nanometers. The lateral resolution is larger, but still less than 500 nanometers. [47]

It must be kept in mind that SIMS is a destructive method as it leaves a crater in the sample surface. It has also been reported that SIMS makes subsequent electrical measurements less favorable, possibly because of the build up of defects in the sample.

3.4 Thermal admittance spectroscopy

Thermal admittance spectroscopy (TAS) is a method used to investigate deep and shallow levels in semiconductors. It is capable of determining parameters such as activation energies, capture cross sections and majority carrier concentrations. Several papers and chapters in textbooks are devoted to explaining the theory behind the method, including Refs. [16, 48, 49]. This outline is, however, to a large extent based on Refs. [50] and [38].

When doing TAS measurements, the capacitance (C) and conductance (G) across a pn-junction or Schottky contact (SC) is measured at several fixed probing frequencies (ω) and variable temperatures. The admittance (Y) is the inverse of impedance, and it is a complex value consisting of an in-phase (G) and out-phase (S) component:

$$Y = G + iS \tag{3.7}$$

where $i = \sqrt{-1}$ is the imaginary unit and $S = \omega C$ is the susceptance.

Schottky diodes were shortly introduced in section 2.1.3, and are used for TAS on ZnO. Not being able to make good Schottky contacts to ZnO was a main obstacle for fruitful research on the material for a long time. Some authors even claimed that depositing working SC diodes to ZnO was more an art than a science [40]. However, there have been huge improvements on this field, and several processes for Schottky contact formation have been developed in the recent years. [21, 51, 52]

It is not straightforward to derive a general expression for the admittance of a SC containing several deep donors, but if the transition between occupied and unoccupied states can be attributed to one defect at the time, the one level approximation can be used with minor corrections. For that reason, only one deep level D_1 and one shallow level with an effective concentration N_{eff} will be considered.

Essential to the understanding of TAS is the concept of trap capture and emission rates. Every donor emits electrons at a certain rate given by the expression

$$e_n^{Di} = \sigma_{Di} T^2 \gamma exp\left(\frac{-E_{Di}}{k_B T}\right) \tag{3.8}$$

where e_n^{Di} is the emission rate, σ_{Di} is the defect's capture cross section, k_B is the Boltzmann constant, and γ is given by

$$\gamma = 2\sqrt{3}(2\pi)^{\frac{3}{2}} k^2 \frac{mm^*}{h^3}.$$

that is, a natural constant times the electron's effective mass.

Consider the situation in figure 3.3. It shows the band diagram of a Schottky diode under reverse and forward bias respectively. In the reverse bias case the deep donor level D_i is completely occupied where $E_F^S > E_{Di}$ and completely empty close to the contact, where $E_F^S < E_{Di}$. Here, E_F^S is the Fermi level energy and E_{Di} is the donor activation energy. During the measurement, a small AC probing signal is added to the DC bias. The donor centers at and near the point $x_i = W - \lambda$ respond to the signal and contribute to the capacitance. This continues as long as $e_n^{Di} >> f$, where f is the probing frequency. As the temperature is lowered, e_n^{Di} decreases, and when $e_n^{Di} << f$,

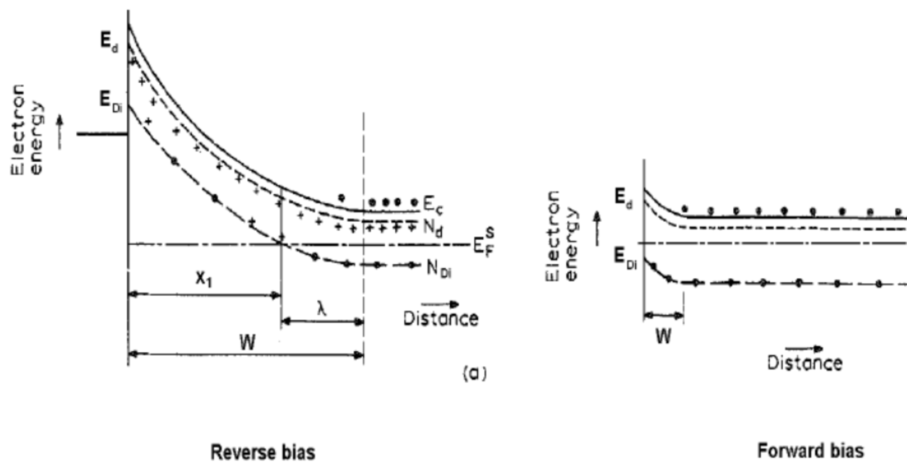

Figure 3.3 – Band diagram of the space charge region when a reverse bias (a) and a forward bias (b) are applied, respectively. In the case of reverse biasing, the Di levels are fully occupied where E_F^S is higher than E_{Di} and completely empty closer to the metal-semiconductor interface. In this region E_F^S is below E_{Di} due to the band bending. On the other hand, by applying a forward bias, the E_{Di} levels can be pushed below E_F^S through the whole space charge region. In this case, the Di centers, if assumed donor-like, are not contributing to the measured capacitance since all neutral.From [50]

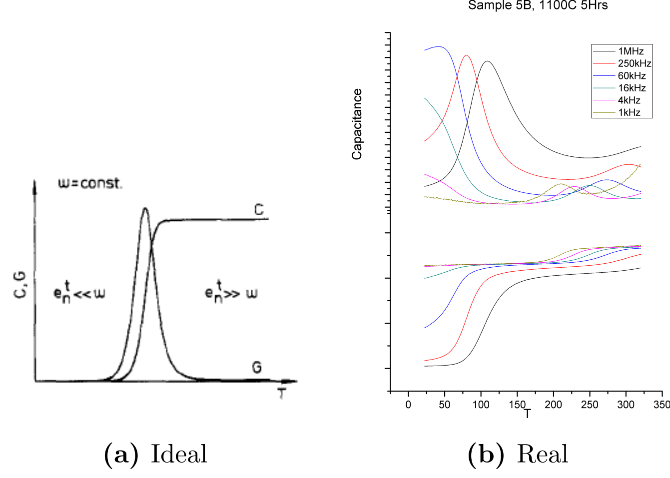

(a) Ideal **(b)** Real

Figure 3.4 – (a) The ideal behavior of the conductance and admittance as a function of temperature when the donor center is frozen out. (b) An example of TAS measurement results in post-growth annealed ZnO. At least two donor levels are present in the sample. Figure (a) is taken from Ref. [48]

the defect D_i no longer contributes to the capacitance. This leads to a drop in capacitance ΔC. Associated with this decrease in capacitance is a peak in conductance. It can be shown that the temperature where the freeze out of the carriers and the associated conductance peak occurs, is related to the energy position of the donor level in the band gap through the expression

$$\frac{2\pi f_T}{\mu(T)T_{max}^{3/2}} \propto exp\left(\frac{-E_d}{kT_{max}}\right) \tag{3.9}$$

where f_T is the probing frequency and T_{max} is the temperature at which the conductance peak is occurring. This equation is used for the freeze out of all charge carriers, i.e. the shallowest donors. From this relation the donor energy can be found as the slope of the $\ln\left[2\pi f_T/\mu(T)T^{3/2}\right]$ vs T^{-1} Arrhenius plot. This is why it is necessary to probe with several frequencies simultaneously.

In order to apply equation 3.9 it is necessary to know the mobility vs temperature behavior, and a power law

$$\mu(T) = \mu_0 T^b$$

is often assumed. Here b depends on the dominant scattering mechanism at the relevant temperature, which can be found with e.g. Hall measurements, or by qualified assumptions.

For conductance peaks occurring at higher temperatures than the freeze out, E_d can be extracted from the standard equation

$$\frac{2\pi f_T}{T_{max}^2} \propto exp\left(\frac{-E_d}{kT_{max}}\right) \tag{3.10}$$

It should be noted that TAS is only suitable for identifying donor levels located below the Fermi level at equilibrium. This means that the shallow level n_d in figure 3.3 will not be detected by TAS.

An illustration of the change in the capacitance and admittance as a function of temperature for the ideal case is shown in figure 3.4. An example of the TAS measurements result for an post-growth-annealed ZnO sample is also shown.

3.5 Hall effect measurements

3.5.1 Basic relations

Most of this section is based on the discussion in Blood and Orton's *"The electrical characterization of semiconductors: Majority carriers and electron states"* [16], Putley's *"The Hall effect and related phenomena"* [53] and the work published by Schifano et al. on TDH measurements using ZnO samples [39, 50].

The Hall effect was first described by E H Hall in 1879 during his investigations of the forces acting on an electrical conductor influenced by magnetic fields [54]. Although he did not fully understand the origin of his observations, Hall proposed the correct relation between the magnetic field and the Hall voltage.

The basic principles of the Hall effect are relatively easy to derive: Consider the circuit in figure 3.5. A rectangular bar of some unspecified material is carrying a current I_x in the positive x-direction. There is also a magnetic field in the positive z-direction, perpendicular to the current. Due to the

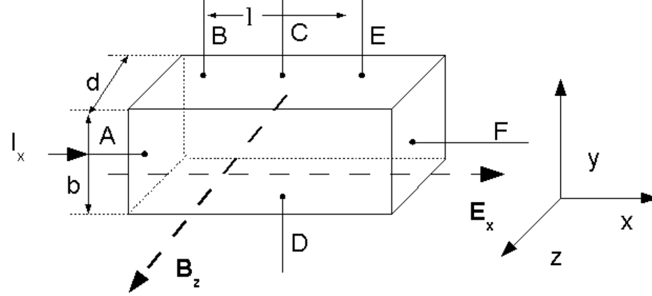

Figure 3.5 – Principal sketch of the circuit used for Hall effect measurements described in the text.

Lorentz force, $\mathbf{F} = q(\mathbf{B} \times \mathbf{v})$, acting on charged particles moving in a magnetic field, the charge carriers are deflected from their straight path. The carriers pile up at the bottom face of the bar, which induces an electrical field in the y-direction, $\mathcal{E}_y$ perpendicular to both I and B. At equilibrium the following relation is valid

$$(\mathbf{B}_z \times \mathbf{v}_x)q = -q\mathcal{E}_y \tag{3.11}$$

and the current flows as before in the x-direction, and the average carrier is not deflected from its straight path. If, for now, it is assumed that all the charge carriers travel with the same velocity $\mathbf{v} = (v_x, 0, 0)$ and $\mathbf{B} = (0, B_y, 0)$, $\mathcal{E}_y \equiv \mathcal{E}_{Hall}$, defined as the Hall field. The transverse electrical field $\mathcal{E}_y$ can be measured by an external voltmeter. The electrical flux through the conductor (again $\mathbf{v}$ is assumed to be the same for all carriers) is

$$\mathbf{j} = -nq\mathbf{v} \tag{3.12}$$

where n is the carrier concentration. Hence from combining equations 3.12 and 3.11:

$$\mathcal{E}_y = \frac{1}{nq} B_z j_x \tag{3.13}$$

The ratio between the electrical Hall field and the magnetic field times the

flux density defines the *Hall factor* R_H,

$$R_H \equiv \frac{\mathcal{E}_y}{j_x B_z} = -\frac{r_H}{nq} \tag{3.14}$$

The derivation above is based on the assumption that that all charge carriers drift with the same velocity. This is generally not true, and a scattering factor r_H is included in equation 3.14 to account for this. This will be discussed in section 3.5.3.

The sign of the Hall coefficient is determined by the charge of the carriers. For positive carriers (holes) the Hall coefficient is positive, and it is negative for negative carriers (electrons). Hall effect measurements can thus be used to determine the carrier type and concentration. It is the simple relation (3.14) between the Hall coefficient and the electron concentration that makes measurements of the Hall coefficient, according to Putley, "the *primus inter pares* amongst the characterization tools for transport properties of conductors." [53]

Hall effect measurements are usually combined with resistivity measurements. The inverse of the resistivity, the conductivity, is given by

$$\sigma = \frac{1}{\rho} = \frac{J_x}{\mathcal{E}_x} = \frac{I_x/bd}{(V_A - V_B)/l} = \frac{I_x}{V_A - V_B} \cdot \frac{l}{bd} \tag{3.15}$$

where b, d and l are the dimensions of the sample as shown in figure 3.5. The drift mobility of the electrons, μ_n, is given by

$$\mu_n = \frac{\sigma}{qn} = -\frac{R_H \sigma}{r} = \frac{|V_C - V_D|}{(V_A - V_B)} \cdot \frac{1}{B_x} \cdot \frac{1}{h} \cdot \frac{1}{r_H} \tag{3.16}$$

The quantity $R_H \sigma$ is usually referred to as the Hall mobility, and differs from the drift mobility by the Hall factor, and is usually slightly larger than the drift mobility.

$$\mu_H = |R_H \sigma| = r_H \mu \tag{3.17}$$

It is important that the contacts to the sample are Ohmic and of good quality, in order to make the contact resistance negligible compared to the resistance of the sample.

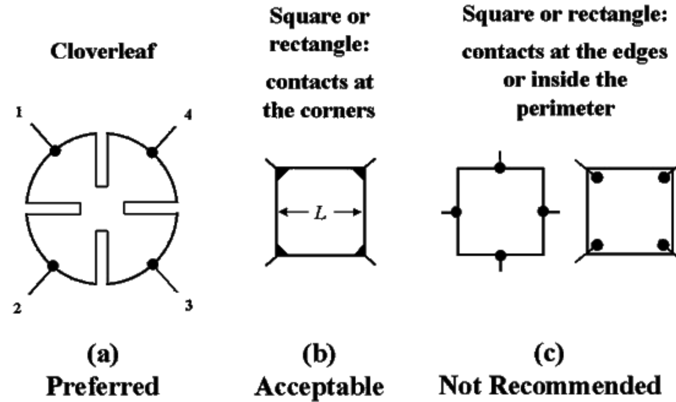

Figure 3.6 – In principle samples of any shape can be used for van der Pauw resistivity measurements, however some geometries are more favorable than others. The clover leaf sample shape is particularly good, but hard to produce in bulk samples. In this work, the contacts are placed on the corner of the samples. From [56]

van der Pauw geometry

Most semiconductor samples are produced as wafers or thin layers. This makes the bar geometry used for the calculation above inconvenient, and the so called van der Pauw geometry is normally used instead for Hall and resistivity measurements. van der Pauw showed that it is possible to measure resistance and Hall coefficients in planar samples of any shape as long as: [55]

1. The sample is uniform in thickness
2. The contacts are at the circumference of the sample
3. The contacts are sufficiently small
4. The surface of the sample is singly connected, i.e. there are no isolated holes in the surface

If contacts are placed along the periphery of the sample and numbered 1 to 4 in a clockwise direction, see figure 3.6, the resistance $R_{12,34}$ is defined as

$$R_{12,34} = \frac{V_{34}}{I_{12}} \tag{3.18}$$

where V_{34} is the potential drop over contacts 3 and 4, and I_{12} is the current through contacts 1 and 2. $R_{34,12}$ is defined similarly. The resistivity is then given by [43]

$$\rho = \frac{\pi}{\ln 2} t \frac{R_{12,34} + R_{34,12}}{2} F. \tag{3.19}$$

In this equation t is the sample thickness and F is a function of the ratio $R_r = R_{12,34}/R_{34,12}$ satisfying the relation

$$\frac{R_r - 1}{R_r + 1} = \frac{F}{\ln(2)} t \operatorname{arcosh} \frac{\exp[\ln(2)/F]}{2}$$

For any symmetrical sample shape, $R_r = 1$, and thus $F = 1$.

3.5.2 Temperature dependent Hall effect analysis

In order to obtain as much information from Hall measurements as possible, they should be performed over a wide range of temperatures, and especially down to as low temperatures as possible. This allows one to observe the freeze out of carriers even from the most shallow defects.

Carrier concentrations

The value of R_H is directly related to the carrier concentration, and it may be valuable to know how the carrier concentration vary with temperature. It is however usually of greater interest to know the concentration of electrical active impurities, both acceptors and donors. This is possible to achieve through temperature dependent Hall measurements, but it requires some calculations.

Consider a non-degenerate semiconductor[1], with the the electrical neu-

[1]A degenerate semiconductor is a semiconductor material with so high doping concentrations that the Fermi level is located outside of the band gap. Thus in a n-type degenerate semiconductor, the region between E_F and E_C is for the most part filled with electrons. A degenerate semiconductor acts like a metal in many respects, but the carrier concentration is usually less than in a proper metal. [15]

trality expression

$$n + n_d = N_d - N_a \qquad (3.20)$$

and the relations describing conduction band and donor level occupancies in terms of the Fermi energy E_F [7]:

$$n = N_C exp\left\{-\frac{E_C - E_F}{kT}\right\} \qquad (3.21)$$

and

$$n_d = N_d\left[\frac{1}{1 + \beta exp\left\{\frac{E_d - E_F}{kT}\right\}}\right] \qquad (3.22)$$

In these equations n is the free electron concentration, n_d is the density of electrons *on* donors, E_d is the donor energy level position, β is a factor that takes the degeneracy of the donor level into account, E_C is the energy at the conduction band edge and N_C is the conduction band effective density of states. Combining these three expressions gives the following expression for n:

$$\frac{n(n + N_a)}{N_d - N_a - n} = \beta N_C exp\left\{-\frac{E_C - E_d}{kT}\right\} \qquad (3.23)$$

Here, $E_C - E_d$ is the donor ionization energy. Solving this for n gives the quadratic equation

$$n^2 + n(N_a + N'_C) - (N_d - N_a)N'_C = 0 \qquad (3.24)$$

where

$$N'_C = \beta N_C exp\left\{-\frac{E_C - E_d}{kT}\right\} \qquad (3.25)$$

Any of these two equations (3.23 and 3.24) may be used to describe the way n varies with temperature. By detailed fitting of parameters to experimental Hall effect data, it is possible to derive values for N_{d_i}, N_a and $(E_c - E_{d_i})$. In principle, the model may be fitted with any number of donors, but it is hard to get unique solutions with too many fitting parameters.

Mobility calculations

As shown in equation 2.4, the mobility is given by the drift velocity of the charge carrier divided by the electric field strength, or

$$\mu = \frac{q\overline{v}}{F} \tag{3.26}$$

This means that low mobility is caused by some 'drag force' from the electron scattering centers, slowing the electrons down despite the force from the electrical field. There are basically two contributions to the electron scattering, impurity scattering and lattice scattering. Each of these may be divided into subcategories, such as ionized impurity scattering, neutral impurity scattering, optical and acoustic phonon scattering etc. Each of these have an unique expression for their relaxation time, and the corresponding mobility term can be calculated through equation 2.3 and added together in an reciprocal manner according to Matthiessen's rule, see equation 2.5.

3.5.3 The Hall scattering factor

The derivation in section 3.5.1 does not take scattering effects into account, and a factor r_H therefore needs to be added to equation 3.14. This factor is a scattering factor and usually takes a value between 1 and 2 depending on the scattering mechanism that limits the drift velocity. Because magnetic fields tend to perturb electron motions, r_H also depends on the magnitude of the magnetic field. It can be shown that if $\mu B_x >> 1$, i.e. in the high field limit, r_H tends towards unity. This makes it possible to determine r_H from experiments by the relation

$$r_H = \frac{R_{H,B=0}}{R_{H,B\to\infty}} \tag{3.27}$$

Very strong magnetic fields are needed for this experiment, often 10 T or higher. To accomplish such strong fields superconducting magnets are required, which is not available in most labs.

For weak magnetic fields r_H rarely differs from unity by more than 20% at room temperature. For many applications r_H can be neglected, and still the error is within the experimental accuracy of the measurement. To get an accurate value of the carrier concentrations and mobilites at low temperatures however, r_H needs to be calculated exactly.

In order to calculate a value for r_H, we once again turn to the relaxation time approximation. As will be shown in the next section, the relaxation

time for individual scattering mechanisms often follow a power law, i.e.

$$\tau(E) \propto E^{-s}, \tag{3.28}$$

where is E is the energy of the charge carrier. This means that each scattering mechanism contributes to r in a specific manner. For example the formula for ionized impurity scattering in the Brooks-Herring approximation follows $\tau(E) \propto E^{3/2}$ giving an analytical value of $r_H = 315\pi/512 = 1.93$. This is valid in the case where ionized impurities is the only source of scattering, otherwise each relaxation time must be added according to equation 2.5. Based on this, the value of r_H can be calculated using the relation [16]

$$r_H = \frac{\langle \tau_{tot}^2 \rangle}{\langle \tau_{tot} \rangle^2} = \frac{\int_0^\infty \tau_{tot}^2(E) E^{3/2} e^{-E/k_B T} dE}{\left(\int_0^\infty \tau_{tot}(E) E^{3/2} e^{-E/k_B T} dE \right)^2} \tag{3.29}$$

3.5.4 Curve fitting and theoretical estimations

In order to extract valuable information from TDH measurements, such as defect densities and donor activation energies, careful curve fitting of the recorded data is required. In this work a Matlab® code written by Dr. Ramòn Schifano was used to deconvolute the experimental data points [38, 50]. The model assumes the presence of one fully ionized, singly charged acceptor (A) and three s-like donors ($D_i, i = 1, 2, 3$), each with an energy level E_{Di} relative to the conduction band minimum. The energy levels of the donors can be measured by for instance TAS or DLTS, or taken from published work on similar samples. It can also be fitted independently, but this requires some caution as the number of free parameters is high.

To fit the mobility data, the relaxation time approximation (RTA) is used. As mentioned in section 2.1.2, this approximation assumes that each scattering event is uncorrelated and can be allocated a relaxation time $\tau_i(E)$ that may be dependent on energy. With this approximation the contribution from each scattering mechanism to the total mobility can be deduced.

In the model used for this work, ionized and neutral impurity scattering, dislocations, acoustic deformation, piezoelectric and polar optical potentials are considered as possible scattering centers. Each scattering mechanism has its own expression for the relaxation time [38]:

- The ionized impurity scattering contributes differently depending on whether the material is highly compensated or not. For lightly compensated materials, the Brooks-Herring approximation gives the most correct estimates for the ionized impurity scattering [57, 58]:

$$\tau_{ionBH}(E) = \frac{16\pi\sqrt{2m^*}(\epsilon_0\epsilon_{r\perp})E^{3/2}}{(N_D^+ + N_A)q^4[\ln(1+\beta^2) - \frac{\beta^2}{1+\beta^2}]}, \tag{3.30}$$

Where ϵ_0 and ϵ_r is the free space and ZnO relative permeability perpendicular to the c-axis respectively, N_A and N_D^- are the acceptor and ionized donor concentrations, m^* is the electrons effective mass in the conduction band, E is the electron's energy and

$$\beta = 2k_B L_D = 2k_B\sqrt{\frac{\epsilon_0\epsilon_r kT}{q^2(N_D^+ - N_A)}}$$

were k_B is Boltzmann's constant and L_D is the *Debye length* defined as stated.

If highly compensated materials are expected, the less common Falicov-Cuevas approximation gives more correct solutions, and the expression is altered to [59]:

$$\tau_{ionFC}(E) = \frac{16\pi\sqrt{2m^*}(\epsilon_0\epsilon_{r\perp})E^{3/2}}{(N_D^+ + N_A)q^4[\ln(1+\eta) + \frac{\eta}{1+\eta}]} \tag{3.31}$$

η is defined as

$$\eta = \frac{2m^*E}{\hbar^2[\pi(N_D^+ - N_A)]^{2/3}}$$

- The neutral impurity scattering relaxation time is given by the expression:

$$\tau_n = \frac{m^*q^2}{80\pi\hbar^3\epsilon_0\epsilon_{r\perp}N_D^0} \tag{3.32}$$

where N_D^0 is the neutral impurity concentration.

- The expression for the dislocation scattering relaxation time is related to the wave vector rather than the energy

$$\tau_{dis}(k) = \frac{8(\epsilon_0\epsilon_{r\perp})^2\hbar^3}{Q^2q^2m^*\lambda N_{dis}}\left(\frac{1}{4\lambda^2} + k_\perp^2\right) \tag{3.33}$$

where N_{dis} is the dislocation density, Q is the charge of the dislocation per unit length, $k_\perp$ is the electron wave vector component orthogonal to the dislocation direction, and $\lambda = \sqrt{k_B T \epsilon_0 \epsilon_{r\perp}/q^2 n}$ is the Debye length. The relation between the relaxation time as a function of wave vector and as a function of energy is in general given by

$$\begin{aligned} &\int\int\int d^3\mathbf{k} v_x^2 \left(\frac{\partial f}{\partial E}\right)\tau(\mathbf{k}) \\ = -\frac{2\sqrt{2m^*}}{\hbar^3}\int_0^\pi d\vartheta \int_0^{2\pi} d\varphi \int_0^{+\infty} &E^{3/2}\sin^3\vartheta\cos^2\varphi \\ &\times\left(\frac{\partial f}{\partial E}\right)\tau(E,\vartheta,\varphi)dE \end{aligned} \tag{3.34}$$

where the electric field appears in the x-direction, v_x is the electron velocity component in the x-direction, and $\delta f/\delta E$ is the derivative with respect to E of the Fermi-Dirac distribution. This makes it possible to derive an expression for the dislocation scattering relaxation time with respect to energy:

$$\tau_{dis}(E) = \frac{3(\epsilon_0\epsilon_{r\perp})^2\hbar^3}{4Q^2 m^* q^2 \lambda^4 N_{dis}} \times \int_0^\pi \left(1 + \frac{8m^*\lambda^2 E}{\hbar^2}\sin^2\theta\right)^{3/2} \sin^3\theta d\theta \tag{3.35}$$

- The acoustic deformation potential scattering's relaxation time is given by

$$\tau_{acu}(E) = \frac{\pi\hbar^4 c_l}{\sqrt{2}m^{*3/2}\epsilon_{acu}^2 k_B T}E^{-1/2}, \tag{3.36}$$

  where c_l is the longitudinal elastic constant and ϵ_{acu} is the deformation potential.

- The piezoelectric scattering relaxation time is given by

$$\tau_{piez}(E) = \frac{2^{2/3}\hbar 2(\epsilon_0\epsilon_{r\perp})}{\sqrt{m^*}2^2 K_\perp^2 k_B T}E^{1/2}, \tag{3.37}$$

  with $K_\perp$ being the piezoelectric coefficient orthogonal to the c-axis.

- Finally, the interaction between the carriers and optical phonons is evaluated by the term

$\epsilon_{r\perp}$	7.77	$\epsilon_{\infty\perp}$	3.70
m^*	0.336	$\epsilon_{ac}(eV)$	3.8
c_l	2.05×10^{11}	$K_\perp$	0.21[a]
$T_{po}(K)$	750[b]	N_{dis}	10^4
$Q(Cm^{-1})$	2.7×10^{-10}		

[a]From ref [44, 60]
[b]From ref [44]

Table 3.1 – List of natural constants used in the mobility evaluation

$$\tau_{op}(E) = \sqrt{\frac{\hbar^2 E}{k_B^3 T_{po}^3}} \frac{1}{\alpha N_q} \times \left(\ln \left| \frac{a+1}{a-1} \right| + e^{T_{po}/T} \ln \left| \frac{1+b}{1-b} \right| \right)^{-1}, \quad (3.38)$$

where T_{po} is the optical phonon equivalent temperature, α is the polar constant and N_q is the mean number of optical phonons at temperature T. That is

$$\alpha = \frac{q^2 \sqrt{m^*}}{4\pi\epsilon_0 \hbar \sqrt{2k_B T_{po}}} \left(\frac{1}{\epsilon_{\infty\perp}} - \frac{1}{\epsilon_{r\perp}} \right)$$

$$N_q = (e^{T_{po}/T} - 1)^-1$$

and

$$a = \left(1 + \frac{k_B T}{E}\right)^{1/2} \qquad b = \mathrm{Re}\left[1 - \frac{k_B T}{E}\right]^{1/2}$$

with $\epsilon_{\infty\perp}$ being the ZnO high frequency permittivity orthogonal to the c axis.

All the material parameters used in the equations above are listed in table 3.1, and are collected from Ref [38] and references therein unless otherwise is stated. It is worth noting that the value $\epsilon_{ac} = 3.8eV$ is an experimental value, not a fitting parameter.

Once the total relaxation time τ_{tot} is known, the Hall scattering factor r_H can be calculated using equation 3.29.

When the values of $r_H(T)$ is calculated, the carrier concentration simulation can be run again with experimental data point corrected for r_H. Based

on this new carrier concentration calculation, a new mobility calculation is done. This continues until self consistency is reached and thus the model gives the actual carrier concentration and mobility values, not the Hall values.

The contact size effect discussed in Ref [61] is also taken into account as a part of the evaluation.

The two layer model

ZnO can, as a result of certain post-growth annealing treatments, show two layer conduction, i.e. the sample is no longer homogeneous, but consists of the normal bulk and a highly conductive surface layer. Look et al. [62] have developed a model that takes this effect into account.

Suppose that the sample with total thickness d consists of not one, but two layers with thickness d_b and d_s, where d_b and d_s is the bulk and surface layer thickness respectively. The apparent, measured carrier mobility and concentration are then, according to Ref. [62] given by:

$$\mu_{meas} = \frac{n_b d_b \mu_b^2 + n_s d_s \mu_s^2}{n_b d_b \mu_b + n_s d_s \mu_s} \tag{3.39}$$

$$n_{meas} = \frac{1}{d} \frac{(n_b d_b \mu_b + n_s d_s \mu_s)^2}{n_b d_s \mu_b^2 + n_s d_s \mu_s^2} \tag{3.40}$$

The thickness of the two layers are in general not known, and they may be hard, if not impossible, to measure in most cases. It can be shown that if it is assumed that $d_s << d_b$ and $d_b \sim d$ the equations simplifies to:

$$\mu_{meas} = \frac{n_b \mu_b^2 + n_s \mu_s^2}{n_b \mu_b + n_s \mu_s} \tag{3.41}$$

$$n_{meas} = \frac{(n_b \mu_b + n_s \mu_s)^2}{n_b \mu_b^2 + n_s \mu_s^2} \tag{3.42}$$

Here, the carrier concentration in the surface layer is normalized to the total thickness of the sample so that it can be plotted on the same axis as the bulk values. The real surface concentration is, however, difficult to evaluate as the surface layer thickness is unknown.

Typically n_b will dominate at high temperatures, but as the donors freeze out, the surface electrons become dominant.

3.5.5 Other galvanomagnetic effects

The electrons in the sample do not drift with the same velocity when carrying current, their velocities varies within a statistical distribution around the average value. From equation 3.11 it is seen that faster electrons follow a different path through the sample than slower electrons. Slower electrons will be more deflected by the electrical field, while faster electrons are more deflected by the magnetic field. This causes one side of the sample to heat up, while the other is cooled down. This is known as the *Ettinghausen effect*, and the Ettinghausen temperature gradient interfere with the Hall effect coefficient in thermoelectric materials. A transverse Ettinghausen-Seebeck field is set up in the sample, and this field is indistinguishable from the Hall field. In addition to this, two more effects known as the *Nernst effect* and the *Righi Leduc effect*, the thermal diffusion analogs to the Hall effect and the Ettinghausen effect causes electrical fields to build up in the sample [53]

There are at least two ways to eliminate these effects. Common to all of them is that they are adiabatic, so if the samples are mounted on a constant temperature heat sink the effects will disappear. A copper sample holder is efficient for transporting heat to and from the sample. If the current is passed through the sample in different directions for each measurement, the build up of heat is also reduced significantly. Combined, these two countermeasures are enough to make the other galvanomagnetic effects negligible compared to the Hall effect and they do not need to be taken into account.

3.5.6 Strengths and weaknesses

The Hall method for measuring carrier concentration and mobility is very applicable because of the simplicity of the experiment. In principle the sample preparation is easy, and if the deposited contacts can be gently removed, the process is non-destructive. If the Hall scattering factor is not taken into account an error up to $\sim 30\%$ is added to the room temperature results. If the carrier concentration is plotted on a log-scale versus inverse tempera-

ture, the donor/acceptor activation energies may in some cases be eveluated directly from slope of the curve.

If the more extensive process of fitting curves to the experimental data is used, extra precautions must be taken. If for example three donors, each with unknown concentration and activation energy, in addition to a compensating acceptor of unknown concentration are included in the calculation, as in this case, a total of 7 unknown parameters must be fitted in the standard one-layer conduction model. To this the two unknown values for surface layer concentration and mobility must be added. Further, there is not full consistency in the literature about all the material parameters listed table 3.1. Based on this, it seems clear that the uniqueness of the solutions achieved are questionable. Therefore complimentary measurements are valuable in order to determine either activation energies or donor and acceptor concentrations for as many defects as possible. TAS is a good method for measuring activation energies, as is photo luminescens (PL) experiments or DLTS for deeper levels. SIMS is excellent for determining impurity concentrations in well known systems, but calibration needs to be made for each new impurity in each material.

In the full calculation the real carrier concentration and mobility, donor and acceptor concentrations and donor energies can be acquired. In summary; when some precautions are made, very valuable information is gained by the Hall effect method.

Chapter 4

Experimental details and results

4.1 Predictions

Based on the work done by Maqsood [4] and other similar works [5, 63], it seemed clear that the lithium, and with it the amount of ionized compensating defects, would decrease significantly after the high temperature post-growth anneals. To get some idea of how this would affect the total mobility, a calculation based on the donor and acceptor concentration and donor energy levels of an as grown ZnO sample [39] was done as a preliminary study. All parameters except the compensator concentration were kept constant, so in most respects the calculation is an oversimplification. For instance the E_3-donor concentration is shown to vary with annealing temperature and actually decreases in concentration at temperatures above 1300 °C [5].

The results of the calculation is shown in figure 4.1, and the donor concentrations and activation energies used are given in table 4.1. It is clear that the compensation ratio is of cardinal importance to the electron mobility in ZnO. From the simulations and the results given by Maqsood [4] it seems reasonable to expect mobilities as high as the 700-800 cm^2/Vs range for the 1500 °C annealed samples, as lithium was expected to be the dominant acceptor.

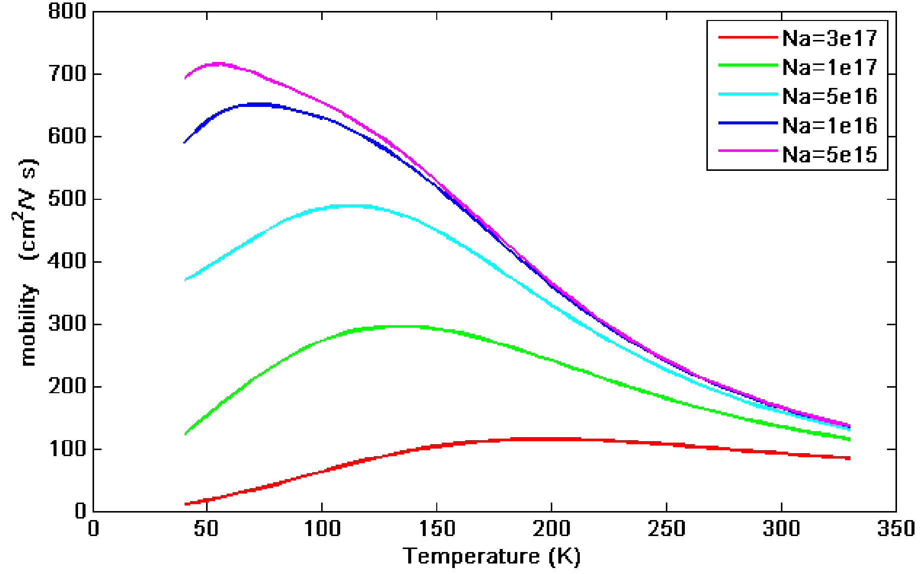

Figure 4.1 – Results of the simplified mobility calculation, showing that ionized compensators contributes significantly to keep the mobility low in ZnO. The Falicov-Cuevas approximation is used for the two calculations with N_A in the 10^{17} range, while the standard Brooks-Herring evaluation is done in the less compensated scenarios.

$\mathbf{N}_{D1}$	E_{D1}	$\mathbf{N}_{D2}$	E_{D2}	$\mathbf{N}_{D3}$	E_{D3}	$\mathbf{N}_{A}$
1.46	29	1.54	44	2.2	307	2.955

Table 4.1 – The donor concentrations and energies used for the simulation. Concentrations are given in $10^{17} cm^{-3}$ and the donor energies are stated in meV. The values are taken from reference [39].

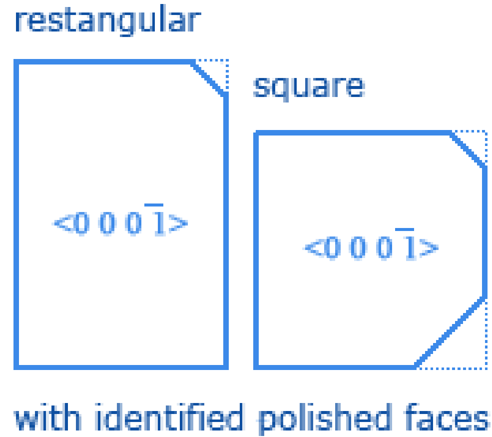

Figure 4.2 – Sketch of the wafers as received from the supplier. The samples used in this work were square with dimensions $(10 \times 10 \times 0.5)mm^3$. From [64]

4.2 Sample details

All the ZnO samples used in this thesis are single crystal wafers supplied by the Russian manufacturer SPC GoodWill [64]. The wafers were hydrothermally grown, and generally rich on lithium due to the manufacturing method. Typically the hydrothermal samples are also rich on aluminum. The wafers are cut perpendicular to the c-axis, and the $\langle 0001 \rangle$ and $\langle 000\bar{1} \rangle$ faces can be determined by identification marks, as shown in figure 4.2. More technical details on the wafers, as given by the supplier, are stated in table 4.2

In total five wafers have been used, see table 4.3 for details on each wafer.

4.3 Sample preparation

4.3.1 Hall samples

The samples used for the Hall measurements were divided into quarters with a diamond cutter. Due to the crystals splitting in a non-ideal direction in some cases and the identification marks, all the samples were not perfectly square. The samples were cleaned in acetone, ethanol and de-ionized water

Parameter	**Value**
Wafer dimensions	$(10 \times 10 \times 0.5) mm^3$
Purity	$> 99.99\%$
Orientation	$\langle 00\bar{1} \rangle \pm 0.25\,\mathrm{deg}$
Resisisivity	$500 - 1000 \Omega cm$
Band gap at RT	3.37 eV

Table 4.2 – The ZnO wafer parameters as stated by the manufacturer.

Sample	**Resistivity, as-received**	**Treatment**	**Used for**
1a	$158 \pm 1.5 \Omega cm$	1500 °C,1hr	Hall, TAS
2a	$4.05 \pm 0.05 \Omega cm$	1500 °C, 1hr	Hall
2b	$4.05 \pm 0.05 \Omega cm$	1500 °C, 1hr	SIMS
3a	$210 \pm 5 \Omega cm$	As-grown	Hall
3b	$210 \pm 5 \Omega cm$	800&1000 °C,1hr	Hall
3c	$210 \pm 5 \Omega cm$	800 °C, 5hr	Hall
3d	$210 \pm 5 \Omega cm$	1200 °C, 1hr	Hall, SIMS
4a	$535 \pm 33 \Omega cm$	1100 °C, 1hr	Hall, SIMS
4b	$535 \pm 33 \Omega cm$	1100 °C, 5hr	Hall, SIMS
4c	$535 \pm 33 \Omega cm$	1100 °C, 15hr	Hall, SIMS
4d	$535 \pm 33 \Omega cm$	1300 °C, 1hr	Hall, SIMS
5a	$0.55 \pm 0.01 \Omega cm$	1100 °C, 1hr	TAS
5b	$0.55 \pm 0.01 \Omega cm$	1100 °C, 5hr	TAS
5c	$0.55 \pm 0.01 \Omega cm$	1100 °C, 15hrr	TAS
5d	$0.55 \pm 0.01 \Omega cm$	1400 °C, 1hr	N/A

Table 4.3 – An overview of the samples used in the experiments. Notice the large variation in resistance. The resistance was measured by four point probe on the $\langle 00\bar{1} \rangle$-face with an eutectic InGa alloy as Ohmic contact on the probes. The measured as-received resistivity does not match with the values given by the supplier in all cases.

in an ultrasonic bath, each for a duration of five minutes. This is from now referred to as the standard cleaning procedure.

The high temperature anneals were performed in an open tube furnace in normal atmosphere (air) with temperatures and durations as given in table 4.3. Due to thermal etching, the surface was quite rough on most samples after the anneal, see figure 4.3 for an example. To deal with this, the samples were mechanically polished with ISO P2000 sandpaper (average grain size of $10\mu m$) and diamond lapping films with grain sizes from $6\mu m$ down to $0.25\mu m$. They were frequently checked in a reflective optical microscope to monitor the process. The polishing is also important to remove the high Li-concentration layer reported by Maqsood [4]. The samples were then cleaned using the standard procedure.

Aluminum is reported to make Ohmic contacts to ZnO [2,65], and for that reason it was chosen over a more complex Ti/Al/Pt/Au sandwich structure used by other authors [39]. 200 nm aluminum contacts were deposited on the corners of each sample using a Leybold e-beam evaporator at a base pressure of 6×10^{-7} mbar, using aluminum foil tape as a mask. These contacts were fragile and got worn of very easily. When wires were bonded to the contacts before measuring, the contacts came off the samples completely. A second attempt to make Al contacts was made after the original contacts had been polished off by diamond lapping films and the samples had been cleaned again. This time 200 nanometers aluminum contacts were deposited by sputtering, and a post-deposition anneal at 200 °C for 60 minutes was done. These contacts adhered better to the samples. Current versus voltage test measurements done diagonally across the wafer from contact to contact showed that the contacts had symmetrical IV characteristics, with marginal deviation from the linear Ohmic behavior. See figure 4.4 for two examples.

However, the contacts showed to high contact resistance and gave too much scatter in the TDH results, so they were removed mechanically. Indium contacts were then soldered onto the sample corners in stead. Indium proved to be an excellent Ohmic contact to ZnO, and very easy to make compared to both e-beam and sputtering deposition.

(a) 1 Hour

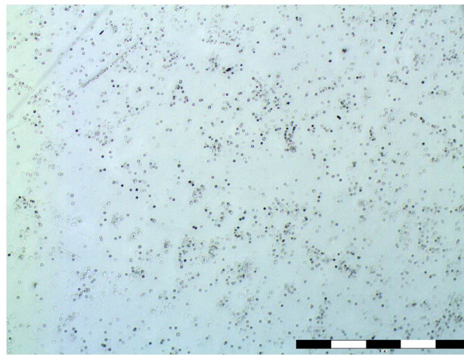

(b) 5 Hours

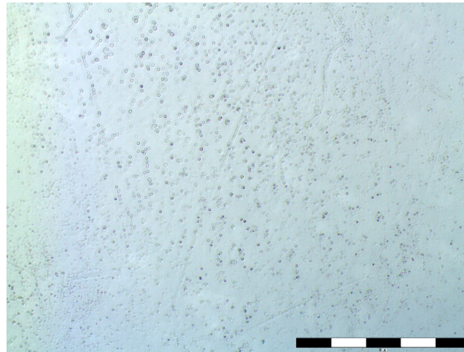

(c) 15 Hours

Figure 4.3 – Optical microscope pictures of wafer 5, annealed at 1100 °C for the 1, 5 and 15 hours respectively. It is seen that small etch pits evolved at the surface over time at these temperatures. The width of the measure bars are increased for visibility, and their full length is equal to 1 mm on the sample surface.

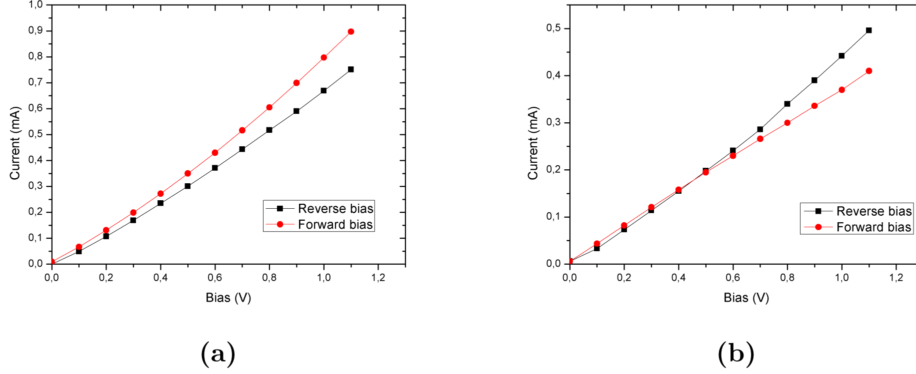

Figure 4.4 – The current-voltage characteristics of sample 3D (a) and sample 4A (b) with aluminum contacts deposited. The curves deviate marginally from an Ohmic behavior.

4.3.2 TAS samples

The samples for the TAS measurements were annealed and polished in the same way as the TDH samples. They were washed in acetone and ethanol before they were immersed in boiling 50% hydrogen peroxide solution for two minutes. This pre-treatment has proven good for depositing Pt and Pd Schottky contacts to ZnO [66, 67], probably because of the formation of a zinc deficient, highly resistive surface layer [68]. 100 nm thick circular Pd contacts, as measured by a quarts crystal deposition monitor, were deposited trough a shadow mask with a Leybold e-beam evaporation system from a 99.999% pure Pd source. The contacts had a diameter of 0.26 ± 0.01 mm, 0.46 ± 0.01 mm and 0.75 ± 0.01 mm. The contacts were deposited on the Zn-polar $\langle 0001 \rangle$-face. After deposition, the samples were annealed at 200 °C for 30 minutes. Silver paste was used as Ohmic back contacts.

4.3.3 SIMS samples

The samples used for the SIMS measurements were the same samples as for the Hall measurements, and no further treatment was done to them except for a standard cleaning.

#	Treatment	ρ as-received	ρ post-annealed	Contact
1a	1hr, 1500 °C	$158 \pm 1.5\Omega cm$	$0.196 \pm 0.003\Omega cm$	InGa
2a	1hr, 1500 °C	$4.05 \pm 0.05\Omega cm$	$0.179 \pm 0.005\Omega cm$	InGa
4d	1hr, 1300 °C	$535 \pm 33\Omega cm$	$0.29\Omega cm$	Indium
3d	1hr, 1200 °C	$210 \pm 5\Omega cm$	$2.7\Omega cm$	Indium
4a	1hr, 1100 °C	$535 \pm 33\Omega cm$	$6.4\Omega cm$	Indium
4b	5hrs, 1100 °C	$535 \pm 33\Omega cm$	$3.4\Omega cm$	Indium
4c	15hrs, 1100 °C	$535 \pm 33\Omega cm$	$1.4\Omega cm$	Indium

Table 4.4 – The samples as-received and post-growth anneal resistivity values. The resistivity was reduced as a result of the heat treatment in all cases, but most for the highest temperatures and longest durations.

4.4 Resistivity measurements

Resistivity measurements were done before and after annealing. The measurements on the as-grown samples were done by linear four point probe on the oxygen polar $\langle 00\bar{1}\rangle$-face with an eutectic InGa alloy as the Ohmic contact, while the measurements on the annealed samples were done both during the Hall measurements using the In contacts in the van der Pauw configuration and with linear four point probe. The results of the measurements are given in table 4.4

It is clear from the results that all the heat treatment reduced the samples resistivity significantly. The stated values were measured at RT, and, as will be shown later, neither the RT mobility nor the acceptor concentration changed much as a result of the post-growth anneals up to 1300 °C. This means that the decrease in resistivity up to these temperatures was mainly caused by donor formation.

4.5 TDH results

The Hall effect measurements presented here were done at the University of Pretoria. The system had a 6 kG (0.6 T) uniform magnetic field, produced by an electromagnet supplied by a HP 60030A power supply unit. A

HP 3245A voltage supply was used to control the current through the sample, and an Agilent 34970A voltmeter was used to measure the Hall voltage. The temperature was monitored and controlled by a Lake Shore 322 temperature controller. The measurements were done in the dark and under vacuum conditions. In order to minimize the effect of thermoelectric heating, unsymmetrical samples and other effects, the measurements were done in four directions for each direction of the magnetic field, eight in total. The sample holder was made of copper, minimizing the adiabatic heating of the sample. The van der Pauw corrections for the lack of total symmetry was done during the measurements of the resistivity. The identity of the samples measured is given in table 4.3 where also their pre-treatment is described. It was not possible to do measurements on samples 3a, 3b and 3c (as-grown, 1 hour anneal at 800 °C and 5 hours anneal at 800 °C) due to too high resistivity, even after sample 3b had been annealed again at 1000 °C for one hour. An increase in resistivity has been reported after heat treatments in this temperature range [4, 63], which may explain this. Sample 5d, annealed at 1400 °C for 1 hr broke during transport, and thus no measurements were done on it.

The results of the Hall measurements are given in figure 4.5. The plots show the Hall mobility, μ_H, and Hall carrier concentration, n_H. The results show an approximately ten times increase in peak mobility, and the room temperature mobility is increased by almost a factor two when comparing the 1100 °C annealed and the 1500 °C annealed samples. Further it is seen that the electron mobility does not change significantly as a function of annealing time at 1100 °C, in contrast to that for the annealing temperature. The carrier concentration increases monotonically as the annealing time is increased, and are highly dependent on annealing temperature, as seen from the 1100 °C and 1300 °C samples, which are cut from the same wafer.

At approximately 100 K and further down in temperature (approximately $10K^{-1}$ and upwards in the 1000/T plot) the carrier concentration is no longer temperature dependent for most of the samples. Instead it stabilizes at some value varying from sample to sample, except for the two 1500 °C samples. This is typical for a two layer conduction behavior. The reason for this layer will be discussed later. The 1500 °C annealed samples do not exhibit two

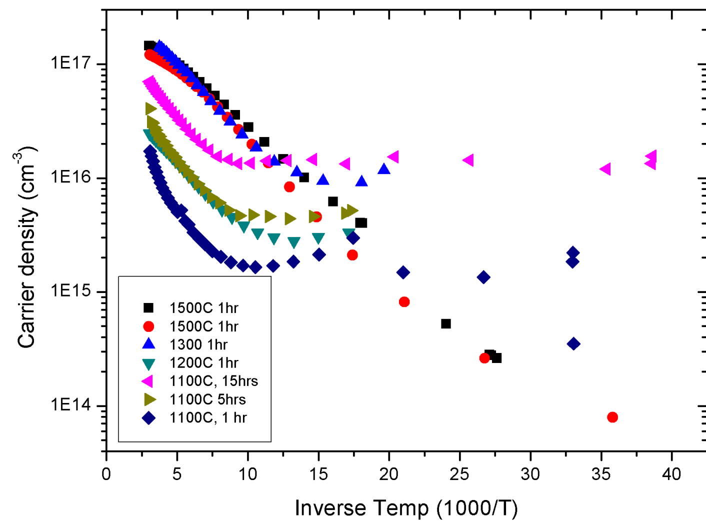

(a)

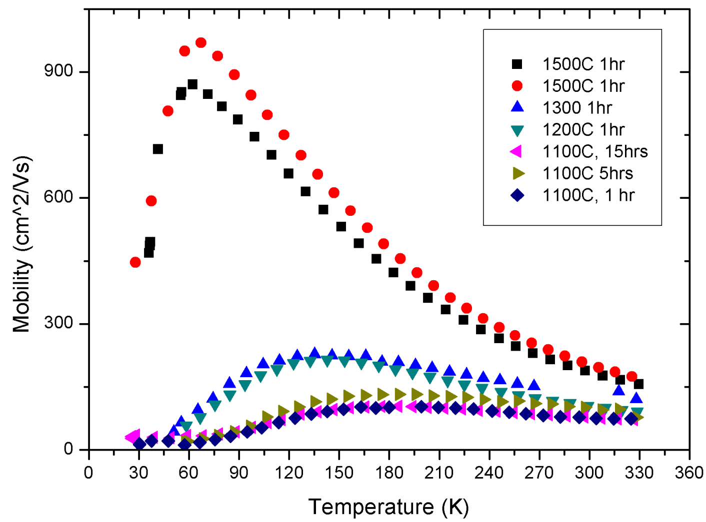

(b)

Figure 4.5 – The Hall carrier concentration (a) and Hall mobility (b). All the samples showed some degree of surface conduction, but the high temperature annealed samples were less affected.

layer conduction to the same extent, but the last few data points deviates from the straight line in these samples as well.

A final possible correlation seen from the figure is the lack of two layer conduction in the 1500 °C samples and their high electron mobility.

4.6 TAS results

TAS measurements were done in order to quantify the activation energies of the donors present in the sample so that the number of free parameters in the Hall calculations could be reduced. The activation energies can be found as the slope of the Arrhenius plot through the relation in equations 3.9 and 3.10.

The measurements were done using the Tiffy setup at the University of Oslo's MiNaLab, which consist of a cryogenic cooler, a Lake Shore 330 temperature controller, and an Agilent 4284A 20-1MHz multi frequency capacitance meter. The measurements were done in the dark and under vacuum conditions, exclusively on the 0.26 mm contacts. It was not applied any reverse DC bias, and a AC signal voltage of 100 mV was used for the probing.

An example of the TAS measurements has already been shown in figure 3.4, and a new example is shown in figure 4.6.

It is worth to notice that the substantial conductance increase, occurring above $\sim$100 K, is overwhelming the expected peak in conductance, according to the theory, associated to the capacitance drop at $\sim$ 200-300 K. This is, most probably, related to the poor Schottky contact performances as suggested by the increase in leakage current with decreasing probing frequencies. To deal with this, the inflection point of the capacitance curve was used to identify the maximum conductance temperature, T_{max}, for each probing frequency. For the freeze out peaks at low temperature, the peak in conductance is used to identify T_{max}. An Arrhenius plot showing all the defect levels found in the samples is given in figure 4.7. The calculated donor energies are given in table 4.5.

The value obtained for E_{D1} is extremely shallow, and this must be seen in context with the Hall measurement results. In the temperature regime where this defects freezes out, the sample is dominated by surface conduction and

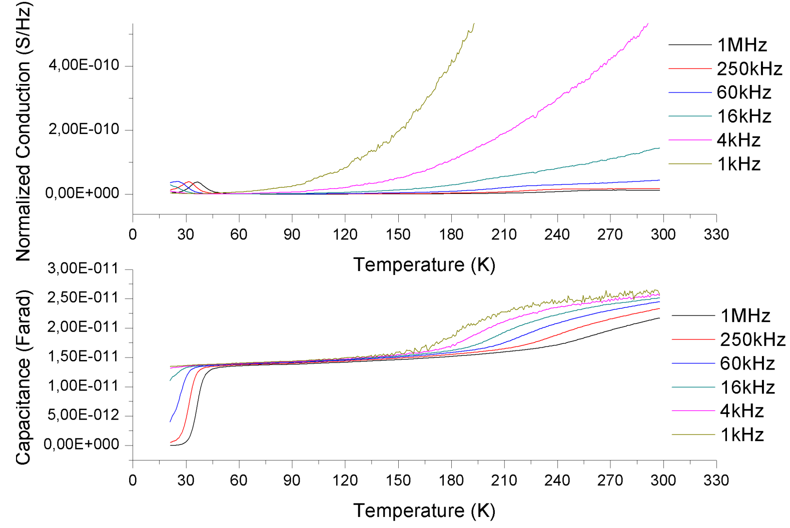

Figure 4.6 – The normalized conductance and capacitance versus temperature for sample 1B, annealed at 1500 °C for 1 hour. The increase in conductance at low probing frequencies id due to the poor performance of the Schottky conctacts.

Sample	Treatment	E_{D1}	E_{D2}
1A	1500 °C, 1hr	7 ± 1	119 ± 5
5B	1100 °C, 5hrs	7 ± 1	120 ± 2
5C	1100 °C, 15hrs	7 ± 1	

Table 4.5 – Activation energies given in meV for the main donor levels detected by TAS measurements.

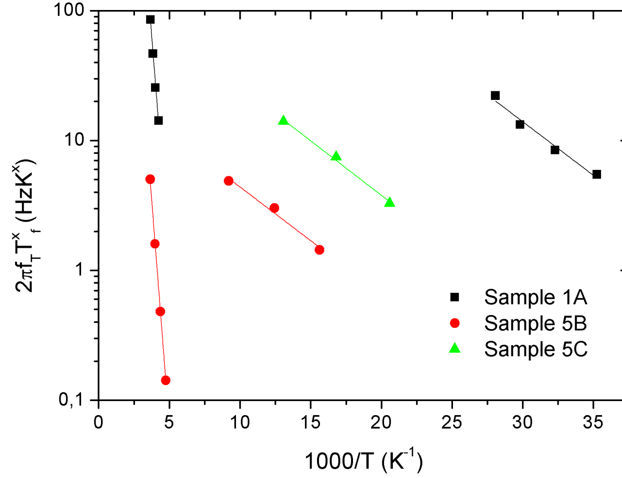

Figure 4.7 – The Arrhenius plot for the activation energies reveals two distinct donors. Ionized impurities are expected to dominate the scattering at the freeze out peaks, so a value of -3 is used for the temperature exponent in that case. In the other cases the exponent is assumed to be equal to -2.

the capacitance drop is probably related to the surface conduction rather than bulk effects. The second donor level, E_{D2} at 120meV, is a known defect from the literature [40]. The prominent E_3-level discussed earlier was not detected, indicating a low concentration of the defect in these two wafers.

4.7 SIMS results

SIMS measurements were performed in order to determine the lithium and aluminum concentrations of the samples. Aluminum is a well known donor in ZnO, and its activation energy is regarded to be ~50meV [39, 69]. The results from SIMS is therefore used directly in the Hall data fitting as the concentration of the E_2 donor. The lithium concentration can be used to estimate the compensator concentration, but other compensators are also likely to be present, such as V_{Zn} [30] as well as other extrinsic acceptors and donors.

The measurements were done using the Cameca IMS 7F Secondary Ion

Sample	**Treatment**	**Al concentration** $[10^{17}cm^{-3}]$	**Li concentration** $[10^{16}cm^{-3}]$
4a	1100 °C - 1hr	1.58 ± 0.03	9.5 ± 0.3
4b	1100 °C - 5hrs	1.39 ± 0.03	7.8 ± 0.2
4c	1100 °C - 15hrs	1.56 ± 0.03	9.5 ± 0.4
3d	1200 °C - 1hr	0.428 ± 0.001	1.5 ± 0.3
4d	1300 °C - 1hr	1.79 ± 0.04	2.79 ± 0.07
2b	1500 °C - 1hr	0.766 ± 0.002	0.11 ± 0.01

Table 4.6 – The bulk aluminum and lithium impurity concentration from samples with the same treatment as in the TAS and Hall measurements.

Mass Spectrometer located in MiNaLab at the University of Oslo, using O_2^+ accelerated to 10keV as primary ions. Ion implanted reference samples with known concentrations of Al and Li were used for the calibration. The crater depth was measured with a Detak 8 stylus profileometer, and a constant erosion rate was assumed for depth calibrations.

The bulk impurity concentration for each sample is given in table 4.6. The values are taken from the depth where the impurity profile stabilizes. The measurements were done at the sample surface midpoint, but only at one point for each sample. Any lateral inhomogeneity would therefore not have been detected. The uncertainty stated in the table is based on the concentration variation versus depth, while the actual overall concentration may vary more than that. It is seen that the Li concentration is reduced as a result of higher annealing temperatures, and it is reduced to as low as $1.1 \times 10^{15}cm^{-3}$ after the 1500 °C anneal.

The aluminum and lithium concentration versus depth profiles are given in figure 4.8. It is clear from the profiles that the post-anneal polishing did not completely remove the highly Li-compensated layer near the surface in all cases. It is also clear that the aluminum concentration in the surface region increases as a result of the heat treatment into as high levels as mid $10^{18}cm^{-3}$ in samples 4a, 4c and 3d. The varying degree of polishing makes it impossible to say anything quantitative about the depth variations of the

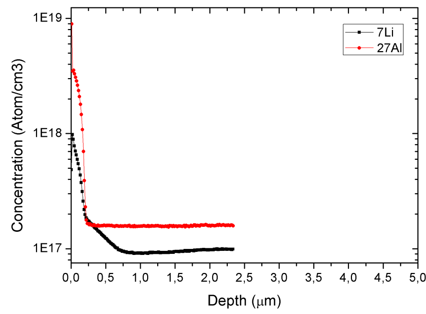

(a) 1100 °C 1 hour

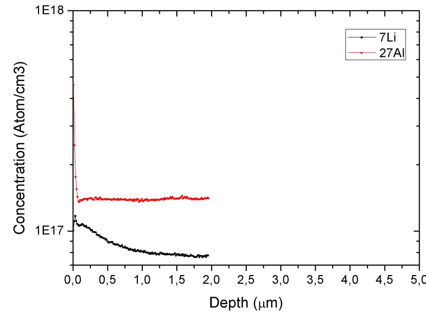

(b) 1100 °C 5 hours

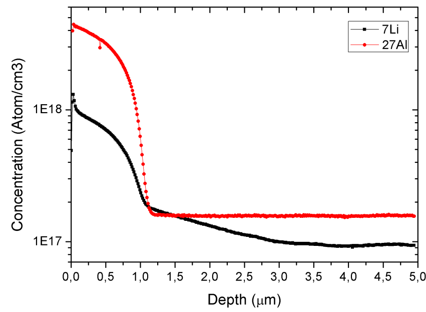

(c) 1100 °C 15 hours

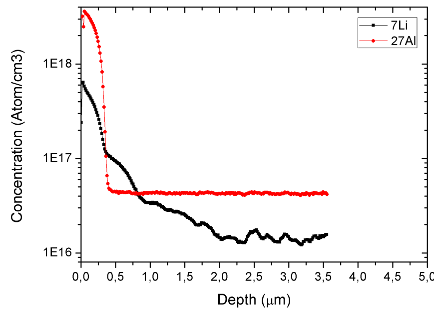

(d) 1200 °C 1 hour

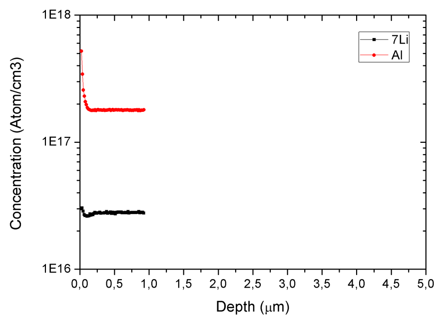

(e) 1300 °C 1 hour

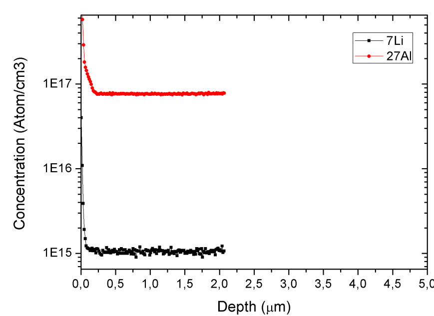

(f) 1500 °C 1 hour

Figure 4.8 – The aluminum and lithium profile for each sample treatment. Note that the samples have been polished mechanically, so that the surface has been worn down to a varying degree. The depths of the impurity profiles are thus not immediately comparable. The samples in figures a,b,c and e are cut from the same wafer, while d and f are cut from two different samples.

impurity diffusion profiles. However, it does seem to be a correlation between the aluminum concentration and the lithium diffusion profile.

It is also worth noting the variation in bulk Li concentration in sample 3d, annealed at 1300 °C for one hour. The Li concentration is well above detection limit, so the distinct variations in Li content with depth are real and not noise in the measurements. This has been observed previously in some samples from the same supplier, and it is believed to be related to *inversion domains* in the material, i.e. domains in bulk of the material where the c-axis is flipped 180° with respect to the rest of the crystal. This may affect the electron mobility and defects observed for this sample [70].

4.8 Fitting of TDH data

The process of fitting Hall data is to a large extent based on fine tuning a set of parameters until a fit is achieved, both for the carrier concentration and the mobility. Many strategies can be applied in order to achieve this, but in this case the following algorithm has been used:

- Add the amount of donors that give a reasonable fit to the experimental carrier concentration vs inverse temperature.
- Do a series of mobility calculations, adding the amount of acceptors and donors that shifts the mobility peak to the right position on the temperature axis. The ionized impurity scattering is highly dependent on temperature, adding acceptors and donors will shift the peak towards higher temperatures and lower the peak value.
- For each iteration, change the values deduced from the experimental data set to updated ones, corrected for the Hall scattering factor r_H.
- Repeat the carrier concentration calculation until a good fit is achieved, and do a mobility calculation based these values.
- When the calculated mobility peak is at the right position with respect to temperature, add the neutral impurity concentration that forces the mobility peak down to the correct value.

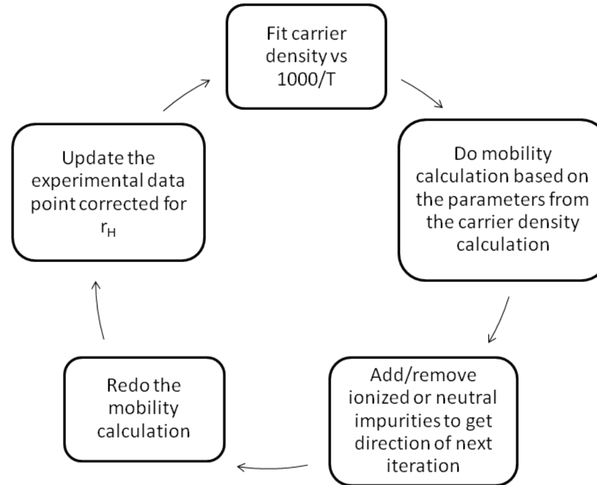

Figure 4.9 – A visual presentation of the iteration method used to fit the TDH parameters.

- In the last iteration the model should be self consistent, meaning that the exact same parameters are used for both the carrier concentration and mobility calculations, nor should the relaxation time calculation change the Hall scattering factor compared to earlier calculations.

See also figure 4.9 for a graphical presentation of the iteration method. As the TAS measurements revealed only one donor energy position, the activation energies are also considered more or less as fitting parameters, and allowed to be varied to some extent, but they are based on previously reported values.

The results of the calculations are given in table 4.7. Uncertainty is not added to the stated values, as they are the ones used for the calculations. They are however not very accurate, especially the concentration of the E_3 donor is hard to quantify since it does not contribute significantly to the carrier concentration in any of the samples, only to limit the peak mobility. The donor at 120meV, however, contributes to a certain degree in the samples where it is present. The activation energy of the shallowest donors, $E_{D1}$and T_1 are also hard to establish, since the measured carrier concentrations are

Treatment	N_{T1}	E_{T1}	N_{D1}	E_{D1}	N_{D2}	E_{D2}	N_{T2}	E_{T2}	N_{D3}	E_{D3}	N_A
1100 °C, 1hr	-	-	2.5	30	1.6	49	-	-	7.8	260	4
1100 °C, 5hrs	-	-	2.3	29	1.4	50	-	-	3.8	240	3.2
1100 °C, 15hrs	-	-	3.9	29	1.6	50	-	-	4.8	240	4.3
1200 °C, 1hr	2.1	12	-	-	0.43	44	0.12	120	-	-	2.3
1300 °C, 1hr	-	-	3.7	25	1.3	50	-	-	5	270	1.9
1500 °C, 1hr	-	-	0.67	31	1.2	44	0.5	120	-	-	0.080
1500 °C, 1hr	-	-	0.93	31	1.5	44	0.9	120	-	-	0.065

Table 4.7 – The parameters used for the Hall curve fitting of the crystal bulk. Concentrations are given in units of $10^{17}cm^{-3}$ and the activation energies in meV. For the samples treated at 1500 °C , the Brooks-Herring approximation is used for the ionized impurity scattering, while the Falicov-Cuevas approximation is used for the remaining samples.

Sample	1a	2a	4d	3a	4c	4b	4a
$n_{surf}[10^{15}cm^{-3}]$	0.6	0.1	15	5	22	8	4
$\mu_{surf}[cm^2/Vs]$	100	100	20	20	25	28	15

Table 4.8 – The surface layer carrier concentration and mobility used for the calculations . The values are considered temperature independent.

dominated by surface conduction at low temperatures. The surface carrier concentration and surface mobility are considered temperature independent, and the values used for each sample is given in 4.8.

The fits for the carrier concentration and mobility are shown in figures 4.10 and 4.11.

The shallow donor level T1 at $E_C - 12meV$, named after Ref. [41], is only found to be present in one sample, the one annealed at 1200 °C. The origin of this defect is not known, but since it is exclusive for this sample, it may have a correlation to the lithium concentration variation found by SIMS. As mentioned, this variation is believed to be related to inversion domains in the sample, which have been identified by transmission electron microscopy in samples with this feature [70].

It is clear from the results that the increase in carrier concentration as a result of longer annealing time, seen in samples 4a, b and c, post-growth annealed at 1100 °C for 1, 5 and 15 hours respectively, is not caused by reduced

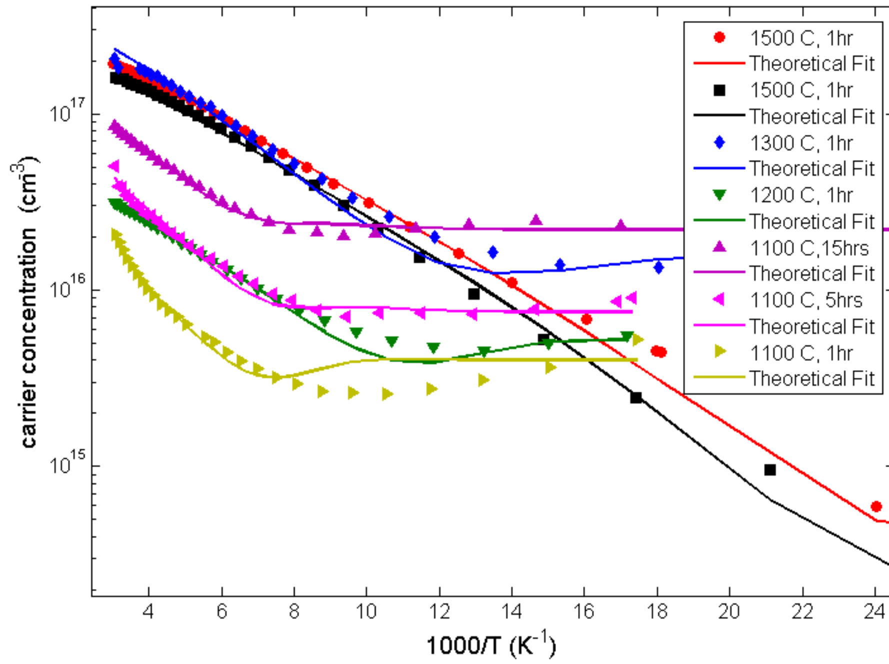

Figure 4.10 – The carrier concentration corrected for the Hall scattering factor and the fitted model for each sample.

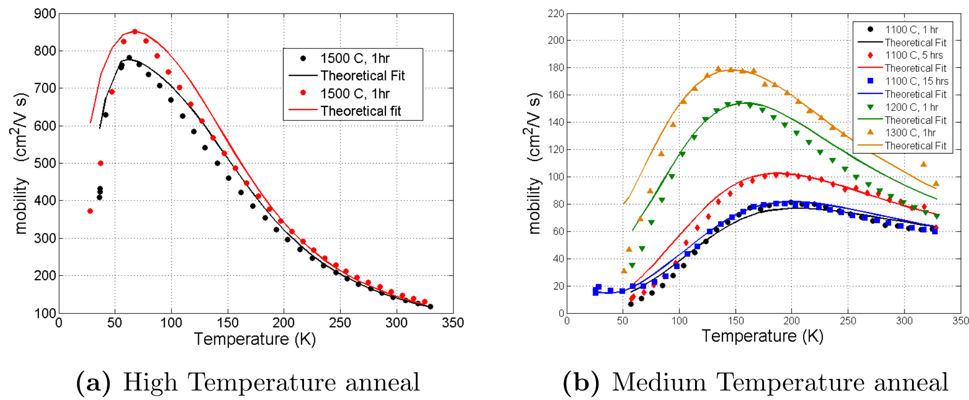

(a) High Temperature anneal

(b) Medium Temperature anneal

Figure 4.11 – The experimental mobility corrected for the Hall scattering factor for each sample, and the theoretical mobility fit corrected for the two layer conduction.

lithium concentration, but the formation of a donor type defect with activation energy of $\sim 30meV$. This defect's concentration has also increased as a result of the 1300 °C anneal. The $E_C - 30meV$ defect has also been observed in as-grown samples [39] and has been attributed to zinc interstitials [24], or a related and more stable (Zn_i-N_O) donor complex [42]. The $E_C - 30meV$ defect is not present in the same concentrations in the samples annealed at 1500 °C. This was also observed by Maqsood [4], as a decrease in carrier concentration between his 1400 °C and 1500 °C annealed samples, despite the observed decrease in Li concentration (Fig. 2.10). The reduction in concentration of the E_1 defect is similar to the $E_C - 300meV$ defect and the total acceptor concentration, whose concentration is also reduced in the 1500 °C samples. This may indicate some correlation between the three defects, but the results presented here are not enough to establish this.

The E_2 defect with a donor level at $E_C - 50meV$ was found in all the samples, and its concentration was fitted to match the SIMS results for aluminum.

The donor with an activation energy of $E_C - 120meV$, also found by TAS, is apparent in three of the samples. The donor is only present in small concentrations compared to the E_3 defect in the other samples, and may thus be present also in the other samples, but remain hidden by the E_3 defects contribution to the carrier density. The fact that the $E_C - 120meV$ is observable in the 1500 °C annealed samples is concurrent with the observation done by Vines et al. [5], that the E_3 defect's concentration is reduced after heat treatments at temperatures above 1300 °C.

The $E_C - 300meV$ E_3 defect was found to give a better fit with a value between 0.24 and 0.27 eV. This is the same value as a defect reported in polycrystalline ZnO [40,71,72]. This defect has not previously been reported to be common single crystal ZnO samples, and it is thus more probable that it is actually the E_3 donor discussed earlier. As the donor do not contribute significantly to the carrier concentration, its activation energy is hard to determine accurately by Hall effect measurements.

In the four samples with the highest compensation ratio, the mobility was dominated by ionized impurity scattering over the whole temperature range up to room temperature, see figure 4.12 for an example. For sample 1a

and 2a, the situation has changed. They are dominated by several scattering mechanisms contributing over most of the temperature range, including optical phonon, neutral impurity and piezoelectric potential scattering, in addition to the ionized impurity scattering.

In all the samples with a high compensation ratio, the calculated and measured values for the total mobility starts to deviate from each other at temperatures bellow approximately 150 K. This is partly because of the two layer conduction of the samples, see figure 4.11, 4.12 and 4.13, but also the two layer correction deviates from the abrupt fall in mobility in this temperature region. Unfortunately, the two layer conduction drowns out any confirming abrupt fall in carrier concentration at the same low temperatures, but the way the mobility behaves may indicate conduction by hopping[1] in this temperature range [44].

[1]Hopping means that current does flow in the conduction band as usual, but is moving in an impurity band inside the band gap. In real space, this correspond to the carriers tunneling from occupied to vacant donor atoms in the crystal. [73]

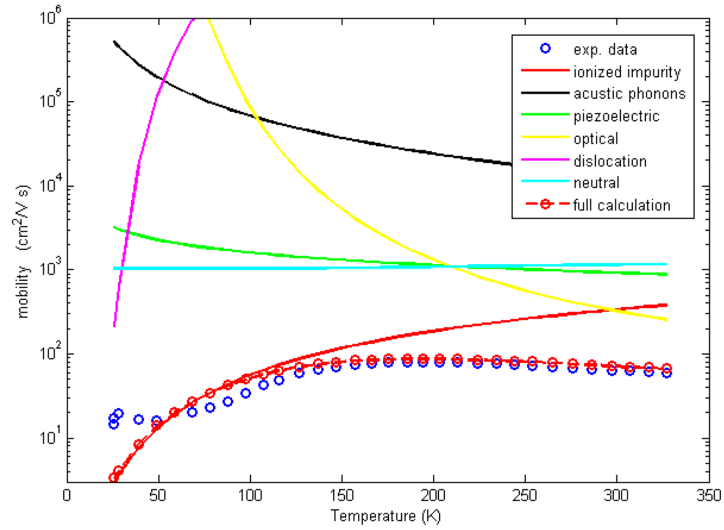

(a) Sample4C

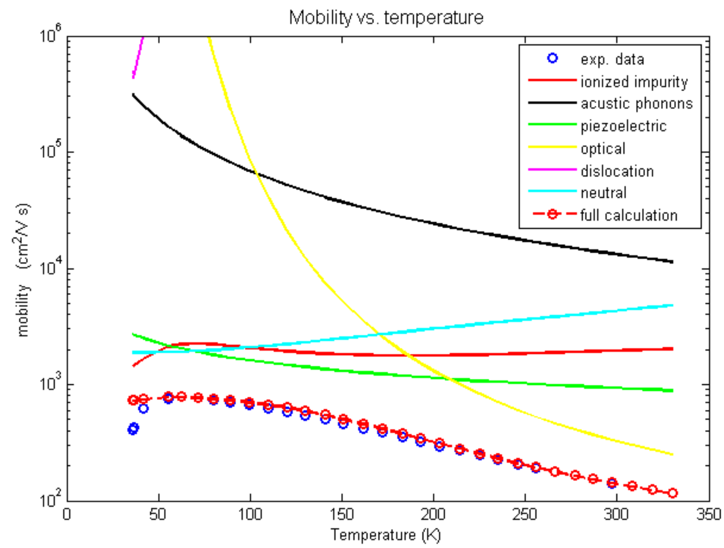

(b) Sample1A

Figure 4.12 – The different scattering mechanism's contribution to the total mobility for sample 4A and 1A.

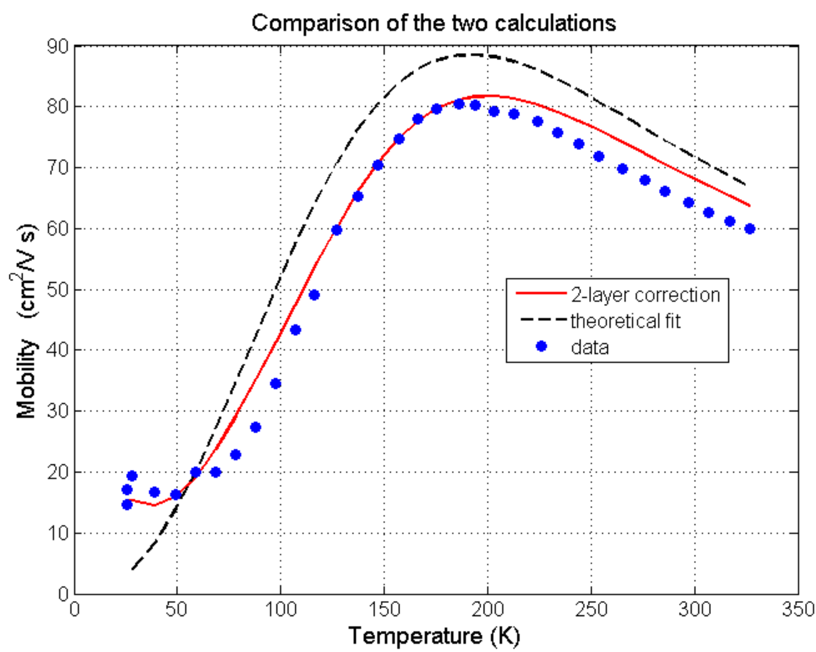

Figure 4.13 – The experimental mobility values measured in sample 4C (1100 °C for 15 hours) corrected for the Hall scattering factor, the theoretical bulk mobility (dashed line) and the same calculation corrected for the two layer conduction.

Chapter 5

Discussion

5.1 Li concentration and mobility

It is clear from the results presented in the previous chapter that both the peak and room temperature (RT) mobility increases significantly as a result of the 1500 °C post-growth annealing. After this heat treatment, the change in both peak and room temperature mobility is clear compared to the 1100 °C anneal.

The RT mobility reached a value of 157 cm^2/Vs after the 1500 °C heat treatment. Both this and the corresponding peak mobility is still far from the intrinsic maximum value of approximately 200cm^2/Vs and 2000cm^2/Vs respectively, calculated by Yang et al. [44]. This is most probably due to the residual impurity atoms, e.g. Al, still present in the samples.

When compared with earlier published work on the same type of as-grown hydrothermal ZnO samlpes [39], both the peak and room temperature mobilitise are somewhat reduced, or at least not increased, as an effect of the 1100 °C anneals. This is surprising, because the lithium concentration is higher in the as-grown samples than in the post-growth annealed ones, but the values obtained for the total acceptor concentration is approximately twice after the heat treatment. Despite variation in defect and impurity concentrations between individual hydrothermal samples, this indicates strongly that a 1100 °C anneal is not sufficient to affect the mobility significantly, and that more acceptors are probably introduced during these heat treatments.

Treatment	μ at RT	Peak μ(T)	N$_{Li}$	N$_A$
As-grown [a]	~ 90	~ 115 (~ 200)	$\sim 16-19$	$\sim 20-30$
1hr, 1100 °C (4)	64	80 (200)	9.5	40
5hrs, 1100 °C (4)	81	102 (196)	7.8	32
15hrs, 1100 °C (4)	64	82 (185)	9.5	43
1hr, 1200 °C (3)	81	154 (153)	1.5	23
1hr, 1300 °C (4)	110-120	170 (135)	2.8	19
1hr, 1500 °C (1)	142	782 (62)	N/A	0.65
1hr, 1500 °C (2)	157	843 (67)	0.11	0.80

[a] From [39]

Table 5.1 – The peak and room temperature mobilities, and the lithium and total acceptor concentrations for the different samples. The mobilities are given in cm^2/Vs and the Li and total acceptor concentrations, N$_{Li}$ and N$_A$ respectively, are given in $10^{16}cm^{-3}$. The temperature where the peak mobility occurs is stated in parenthesis. For comparison the original wafer number is also given in parenthesis. The data is collected from the measured data points, but is corrected for r_H, which is based on calculations.

See table 5.1 for a full summary of the mobilities for each sample.

Before an in-depth analysis of the results presented in table 5.1 can be done, the surface conduction's contribution to the total measured mobility as given by equation (3.41) must be examined. This is necessary in order to rule out the possibility that the high surface conduction observed in the samples heat treated at 1100-1300 °C is drowning out the bulk mobility values. To check this, a series of mobility calculations based on the parameters deduced for sample 4a was done, using an acceptor concentration of $1.25 \times 10^{17} cm^{-3}$, with the value of μ_{surf} as the only variable. The results are given in figure 5.1, and shows that with the parameters used, the measured mobility differs from the bulk value by less than 20%. This is assumed to be valid also for the real measurements, and it is thus established that the bulk mobility is dominating the measured values. For values of μ_{peak} higher than 200 cm^2/Vs, the shape of the curve changes, and that was not observed in the measurements.

It is a clear correlation between the Li concentration and the peak mobil-

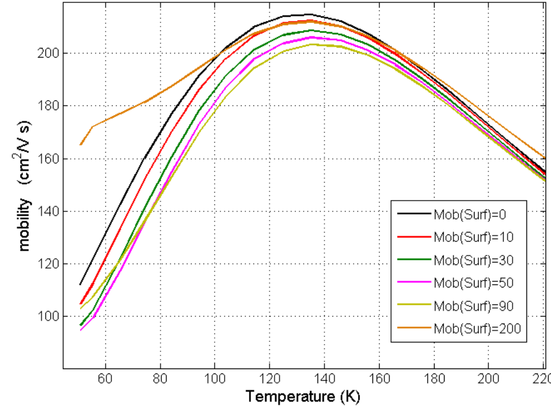

Figure 5.1 – The calculated total mobility for a set of donor and acceptor parameters based on the ones used for sample 4a, with the surface layer mobility as the only variable

ity when looking isolated at the 1100 °C and 1500 °C heat treated samples. The intermediate samples, however, do not follow the trend predicted in the preliminary study presented in figure 4.1. This is because the assumption that Li, present as Li_{Zn}^{-}, is the dominating acceptor in all the samples seems to be incorrect.

Figure 5.2 shows the total acceptor concentration, N_A, the measured Li concentration, N_{Li}, and the difference between them, ΔN_A. In the part of the diagram named Region I, both N_{Li} and N_A remain unchanged as a result of longer annealing times at 1100 °C. Interestingly, the ratio between N_{Li} and N_A is 1/4 in all three cases. The total carrier mobility is limited by ionized impurity scattering in the low temperature regime, which is the temperatures where the mobility peaks occur for these three samples. In the model used to estimate the ionized impurities' contribution to the total relaxation time, equations (3.30) and (3.31), only singly charged scattering centers is assumed. The full expression is however also dependent on the charge of the defect by a factor $1/Z^2$, where Z is the defects effective charge. This means that if lithium is the dominant acceptor in ZnO, but present as part of a doubly negatively charged acceptor complex, the model used to calculate the ionized impurity scattering and from that the acceptor concentration is overestimated by a factor 4.

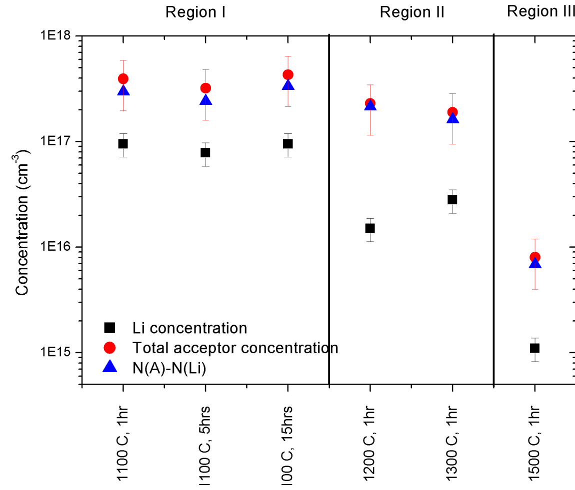

Figure 5.2 – The total acceptor and lithium concentration in each sample. The triangles, $\Delta N_A = N_A - N_{Li}$, represent the difference between the total acceptor concentration, as determined by TDH, and the Li concentration, as measured by SIMS.

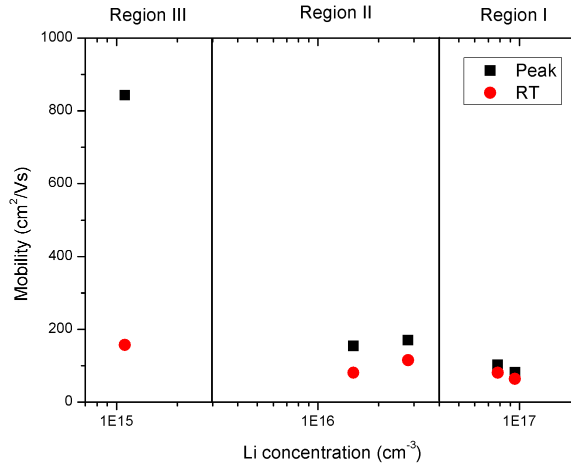

Figure 5.3 – The relation between the Li concentration in the samples and the room temperature and peak mobility. The mobility seems to be marginally affected by the Li concentration above the $10^{16} cm^{-3}$ region, but in the $10^{15} cm^{-3}$ range the peak mobility has increased by a factor ten compared to the lowest mobilities.

In Region II, however, Li is diffusing out of the sample bulk, and its concentration is reduced by a factor 2.8-6.3, as measured by SIMS. The slight increase in electron mobility at these temperatures may be attributed to the reduction of Li in the samples. The total acceptor concentration, on the other hand, is only reduced by a factor 1.4-2.3. This development invalidates the doubly charged Li acceptor complex hypothesis. In stead it must be concluded that a second acceptor is present in high concentrations in addition to Li_{Zn} in the samples examined. The identity of this acceptor is unknown, but as ΔN_A in the samples examined here (see figure 5.2) is higher than the as-grown samples investigated in Ref. [39] ($\sim 1 - 1.5 \times 10^{17} cm^{-3}$), it can not be ruled out that it is partly introduced during the 1100-1300 °C heat treatments.

In Region III, where the annealing temperature is 1500 °C, the total acceptor concentration is reduced by more than one order of magnitude compared to the other two regions. This shows that the unknown acceptor is also leaving the sample at this temperature, in parallel with the Li out-diffusion. It is not until the reduction in this acceptor's concentration occurs that the electron mobility increases significantly, as can be seen when comparing the results in figure 5.2 to those presented in figures 5.3 and 4.5.

From this it must be concluded that Li_{Zn}^-, acting as a compensating acceptor, is not the limiting factor with regards to the electron mobility in the hydrothermal ZnO samples examined, post-growth annealed at temperatures up to 1300°C*.* In stead, the mobility is limited by another acceptor which diffuses out of the samples at 1500 °C. The identity of this acceptor is hard to establish, but its behavior, as shown in figure 5.4, indicates that it is intrinsic, since the most prominent impurity defects, except Li, are shown to be very stable in concentration even after 1500 °C heat treatments [5, 6]. The most prominent intrinsic acceptor in ZnO is shown to be the zinc vacancy, V_{Zn} [30]. I suggest that this defect is the dominant acceptor also in the hydrothermal samples examined, not the residual lithium as previously assumed.

This is a bold hypothesis, as the concentration of V_{Zn} is reported to be much lower than what is found here. For instance, Tuomisto et al. [30] determined it to be $\sim 2 \times 10^{15}$ in samples grown by the seeded vapor phase

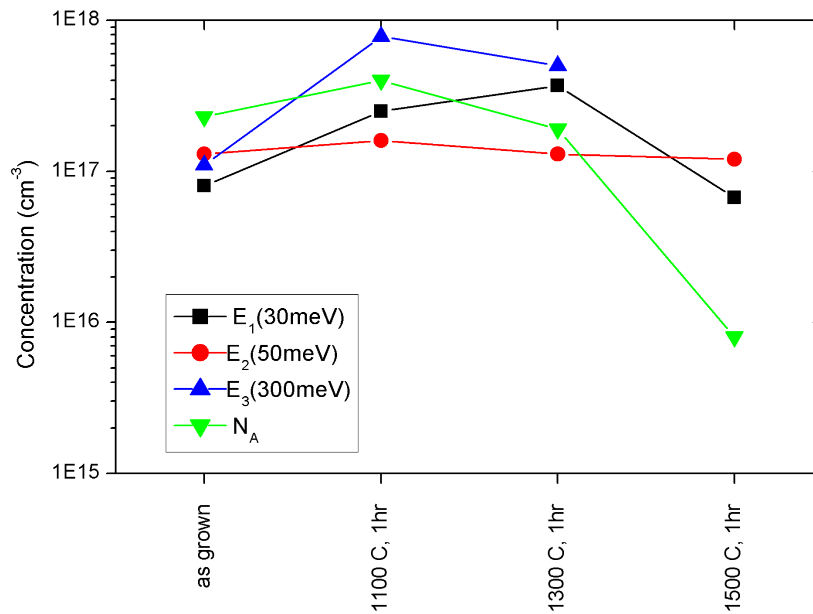

Figure 5.4 – The development of the most prominent donor defects' and the total acceptor concentrations, determined by TDH measurements, as a function of annealing temperature. The as-grown data is adapted from Ref. [39]. The E_3 donors concentration after the 1500 °C anneal was to low to be detected by TDH, but it is probably in the 10^{15} cm^{-3} range.

technique, while it has been reported to be $\sim 2 \times 10^{16}$ in contactless chemical vapor transport grown samples [74]. Further investigations of hydrothermal samples are thus needed to support or falsify this hypothesis.

If V_{Zn} is indeed the dominant acceptor, the reduction of both the total acceptor concentration and the $E_C - 30meV$ donor, suggested by Look et al. to be Zn_i related [42], can be explained by a simple Frenkel defect recombination

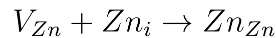

$$V_{Zn} + Zn_i \rightarrow Zn_{Zn}$$

Zn_i is very mobile and unstable even at room temperature [75,76], and therefor the mechanism we observe can not be as simple as in the chemical equation above. What may have happened during the 1500 °C annealed, is that the proposed (Zn_i-N_O) acceptor complex [42] decomposes, followed by the recombination of the Frenkel defect pair as shown above.

5.2 Origin and effects of the surface conduction

It is seen from the TDH data presented in the last chapter that a degenerate conductive layer is present in all the samples examined, although to less extent after the 1500 °C anneal. The SIMS analysis indicates that accumulation of aluminum in the surface region may be the cause of this. ZnO is known to have a highly reactive surface, and during high temperature anneals impurities from the bulk, e.g. aluminum, lithium or hydrogen, may get trapped at and near the surface. Impurities from the ambient, especially hydrogen, may also get adsorbed during the sample treatment.

D.C. Look et al. were amongst the first ones to discuss the origin of the degenerate conductive layer [62]. They attributed the origin of the surface layer to hydrogen, as X-ray photoelectron spectroscopy (XPS) revealed the presence of OH bonds in the surface, and the fact that O_2-plasma treatment and high energy electron radiation reduced the surface conductivity. Further, for annealing temperatures of 800 °C and higher, the surface carrier concentration was found to decrease, which is consistent with the observation that

hydrogen is shown to effuse from the sample at high temperatures [77]. In our case the samples have been treated at much higher temperatures than this, and for that reason this explanation seems insufficient, and another explanation is needed. In a later article presented by the same author [78], it was shown that a degenerate conductive layer is present in samples made from all commercially available growth methods. In a third article [79] TDH characterization is done in combination with SIMS on three hydrothermal ZnO samples after anneals at 600 °C in nitrogen and forming gas (5% H_2 in N_2) atmospheres. The last sample was annealed at 930 °C in order to reduce the hydrogen content before a 600 °C anneal in forming gas was performed. The last treatment was designed to reduce the hydrogen concentration in the bulk before introducing new hydrogen from the ambient. All three anneals lasted for 30 minutes. The experiment showed that the *bulk* resistivity was decreased as a result of the forming gas treatment. This was mainly caused by acceptor passivation. The *surface* resisitvty however showed a distinct *increase*, showing that hydrogen did not contribute to the surface conductance in this case. SIMS measurements showed a group III element profile similar to the one reported in the previous chapter, reaching 80 nm into the unpolished samples. The profile was thus shallower than the one reported here, but the anneal was also for shorter times and at lower temperatures. The group III element concentration was as high as the low $10^{20} cm^{-3}$ range at the surface, but fell to $10^{18} cm^{-3}$ during the first 15 nm. The conclusion in Ref. [79] is that the surface conducive layer in hydrothermal samples after the post growth anneals is mainly due to group III ions, not H or any native defect related donors.

When examining at the SIMS results in Fig. 4.8 compared to the Hall effect results in Fig. 4.5, the correlation between the normalized surface layer carrier concentration and the integral of the aluminum profile fits for three of the samples dominated by surface conduction, but not for sample 4b, annealed at 1100 °C for five hours, and sample 3d, annealed at 1300 °C for one hour. The SIMS analysis that the Al concentration is only accumulating the first 100 nm or so for both samples. One possible reason for this is that the post-anneal polish was not uniform in depth. Maqsood describes the sample surface after the same polishing procedure as “a smooth landscape with no

trees" after white light interferometry examination of his samples [4], i.e. the samples were smooth, but with large peak to valley height differences. The SIMS measurement were only done at an area of $150 \times 150 \mu m^2$ per wafer, so inadequate sample surface uniformity will not be detected. The samples were examined by optical microscope to ensure that there were no obvious scratches, but a vertical variation of a few micrometers can not be ruled out. Under this assumption, the minimum surface layer thickness can be calculated from the Hall effect measurements, and compared with the integral of the aluminum profile measured by SIMS where present.

The donor concentration in the surface layer in unit of cm^{-3} is given by the working equations below. Their detailed derivation is given in [78]. They are based on the assumption that the mobility of the charge carriers in the surface layer is limited by ionized impurity scattering, and derived from the Brooks-Herring non-degenerate expression:

$$N_{D,surf} = \frac{1}{2}\left(\frac{7.647 \times 10^{17} T^{3/2}}{\mu_{H,meas}(T)\left\{\ln[1 + y(d_{surf})] - \frac{y(d_{surf})}{1+y(d_{surf})}\right\}} + n_{meas}\frac{d_{total}}{d_{surf}}\right) \tag{5.1}$$

while the surface acceptor concentration is given by

$$N_{A,surf} = \frac{1}{2}\left(\frac{7.647 \times 10^{17}[(cm\ Vs\ K^{3/2})^{-1}] T^{3/2}}{\mu_{H,meas}(T)\left\{\ln[1 + y(d_{surf})] - \frac{y(d_{surf})}{1+y(d_{surf})}\right\}} - n_{meas}\frac{d_{total}}{d_{surf}}\right) \tag{5.2}$$

In both equations, T is the absolute temperature, n_{meas} and N_a are stated in cm^{-3} and μ_{meas} in cm^2/Vs. The number $7.647 \times 10^{17} 10^{17}[(cm\ Vs\ K^{3/2})^{-1}]$ is the product of several natural constants and material parameters as stated in the Brooks-Herring equation. In both cases

$$y(d_{surf}) = 1.293 \times 10^{-6} cm \left(n_{meas}\frac{d_{total}}{d_{surf}}\right)^{1/3} \tag{5.3}$$

By setting $N_{A,surf} = 0$, the obvious minimum acceptor concentration, equation 5.2 can be solved for d_{surf}, giving the minimum surface layer thickness. Doing this for sample 4c (1100 °C, 15hrs anneal), using the measured

values at $T = 38.9K$: $n_{meas} = 1.44 \times 10^{16} cm^{-3}$, $\mu_{meas} = 30.2 cm^2/Vs$ and $d_{total} = 500\mu m$, the minimum surface layer thickness is estimated to be $d_{surf} = 1.26\mu m$. This is in close agreement with the width of the aluminum profile, which is measured by SIMS to be $1.2\mu m$. Using the acquired value for d_{surf}, N_d is calculated to be $1.45 \times 10^{19} cm^{-3}$. These two values constitute a 'square' surface profile, and the product of them gives a sheet concentration of $(1.45 \times 10^{19} cm^{-3})(1.25\mu m) = 1.83 \times 10^{15} cm^{-2}$.

Doing the actual integration on the aluminum profile gives a sheet density of aluminum equal to $2.9 \times 10^{15} cm^{-2}$. It is quite natural that the Al density as measured by SIMS is higher than the estimated value, since the Li compensation is not taken into account. Further, the values obtained by SIMS is the chemical concentrations, not the electrically active Al donor concentration. The sample surface inhomogeneity will also influence the results. Similar conclusions can be made for the other two samples dominated by surface conduction and having a clear aluminum profile, proving evidence that the surface conduction observed is mainly due to aluminum accumulation in the vicinity of the sample surface.

5.3 The Li and Al Diffusion correlation

An interesting finding is the apparent correlation in the the lithium and aluminum concentration profiles. First, however, the origin of the aluminum accumulation at the sample surface must be established. One possible explanation introduction during the contact deposition. However, since the aluminum was deposited after the high temperature anneal and subsequent polishing, this seems unlikely. If it was the case one would expect a more similar concentration profile in each sample, since they received the same treatment after the deposition. Further, the central parts of the sample surface was covered by aluminum foil tape during the deposition, and the 30 min 200 °C post-deposition heat treatment would not be sufficient fro aluminum diffuse to diffuse to the center of the sample and several hundred nanometers into it.

Hence, it appears likely that the surface accumulation of aluminum was introduced during the anneal. Bulk aluminum concentration is, in contrast to

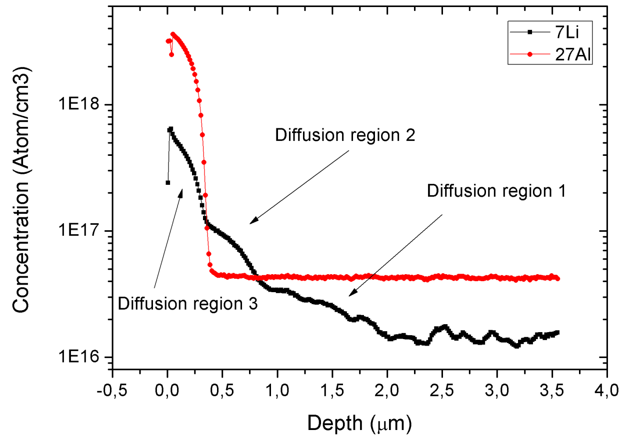

Figure 5.5 – The lithium and aluminum SIMS profile of sample 3D, annealed at 1300 °C for 1 hour.

that of lithium, known to be unaffected by high temperature treatments [5,6]. Thus trapping in the sample surface region of Al diffusing from the can also be excluded.

Most likely the samples have been contaminated by the alumina, Al_2O_3, boat it was contained in during the high temperature anneal. If this is the case, special precaution needs to be made in order to avoid this in the future. Paying extra care placing the face to be examined upwards during annealing is recommended. Even though the in-diffusion of aluminum is undesirable, it is interesting to see how the high Al concentration affects the lithium concentration depth profile, see figure 5.5. Especially the transition between regions two and three in the figure is tangible. Lithium seems to act as a charge compensator when its concentration is less than that of aluminum, while it diffuses readily when it is more abundant than aluminum. The retarded diffusion of Li in the Al-rich region suggests that the migration of the two elements is mediated by the same type of intrinsic defect, like for instance the zinc vacancy. In addition, a dependence of the Li diffusion on the E_F position (the sample is highly n-doped in the Al-rich regions) can play a role.

5.4 Suggestions for future studies

In section 5.1 it was argued that lithium was not the dominant ionized acceptor in the samples heat treated at 1100-1300 °C , and that this acceptor is the limiting factor for the electron mobility in those samples. This acceptor remains unidentified, even if it was suggested that it is V_{Zn}, and further investigation of its origin will be necessary in order to shed more light on the electrical properties of HT ZnO. The missing annealing temperature at 1400 °C would have been useful in order to determine more precisely in which temperature interval the defect is beginning to diffuse out of the material. The breaking of this sample during transport is yet an example of the validity of Murphy's law.

A very recently published article on hydrothermal ZnO from the same supplier, treated with the same post-growth annealing procedures as here [6] showed a peak electron mobility of $1180cm^2/Vs$ already after the 1300 °C anneal. This is a different result than what is presented here, and further investigations are needed. It does however imply that sample variations may be significant in the material investigated. It is for instance possible that the acceptor in the samples examined by Vines was passivated to a larger extent by hydrogen.

In order to establish the activation energies of the shallowest donors in the sample more accurately, the conductive surface layer will have to be removed by further polishing. This is easy to accomplish, and once an experimental set up is installed in our lab, new TDH measurements on more homogeneous samples can be carried out to get a more precise characterization of the material. If the two layer conduction is still present after extended polishing, a more complete estimation of the surface carrier's contribution to the measured carrier concentration and mobility can be implemented in the computer program used to fit the TDH data. Equations (5.1, 5.2 and 5.3) can be used for such an estimation, combined with a simplified mobility calculation for the surface charge carriers, for instance only based on ionized impurity scattering as stated in the Brooks-Herring equation (3.30).

The highest peak mobility measured, in the samples annealed at 1500 °C, is quite low compared to the highest mobilities measured previously in ZnO

[24, 42] and the intrinsic maximum electron mobility estimated by Yang et al [58], both near $2000cm^2/Vs$. Aluminum is a well known ionized impurity in HT ZnO, and a similar study to this one, where the Al impurity density was varied over several orders of magnitude between the samples, would be very interesting. Such samples could be manufactured in thin films, e.g. by the sputter deposition method and characterized by the same methods as presented here.

Chapter 6

Conclusion and summary

In this work, hydrothermally grown n-type ZnO samples purchased from SPC Goodwill have been heat treated at temperatures up to 1500 °C, and electrical characterization by means of TDH and TAS measurements have been preformed. The samples were also investigated by SIMS to identify the Li and Al content of the samples.

It was found that the room temperature and peak electron mobility increased significantly as a result of the 1500 °C post-growth anneal, while the variation was only marginal at lower temperatures. Five main donors were found to contribute to the n-type behavior of the material, approximately 12, 30, 50, 120 and 300 meV below the conduction band respectively. All were previously observed donors.

The free charge carrier concentration increased by one order of magnitude as a result of the heat treatments, mainly due to the formation of donors with energy position $E_C - 30meV$ in the band gap. It was also confirmed that the concentration of the prominent E_3 defect, positioned at $E_C - 0.3eV$ in the band gap, is reduced as a result of the annealing at 1500 °C.

The samples annealed at 1100-1300 °C was to a large extent dominated by surface conduction. This is observed in most ZnO samples, but usually only at very low temperatures ($\leq 30K$), while it was observed already at $\sim 100K$ in the samples examined here. It was established that this is mainly due to Al contamination introduced during the annealing step in the samples examined.

A big leap in peak and room temperature electron mobility was revealed as a result of the 1500 °C heat treatment, compared to the treatments at lower temperatures. This increase in mobility is believed to be caused by the vanishing of an acceptor defect other than Li_{Zn}, which diffused out already at 1000 °C. The identity of this other defect remains undetermined and subject to further studies, but V_{Zn} was tentatively suggested.

Bibliography

[1] K. L. Chopra, P. D. Paulson, and V. Dutta. Thin-film solar cells: an overview. *Progress in Photovoltaics: Research and Applications*, 12(2-3):69–92, 2004.

[2] Ü. Özgür, Ya. I. Alivov, C. Liu, A. Teke, M. A. Reshchikov, S. Doğan, V. Avrutin, S.-J. Cho, and H. Morkoç. A comprehensive review of ZnO materials and devices. *Journal of Applied Physics*, 98(4):041301, 2005.

[3] D. Chakraborti, S. Ramachandran, G. Trichy, J. Narayan, and J. T. Prater. Magnetic, electrical, and microstructural characterization of ZnO thin films codoped with Co and Cu. *Journal of Applied Physics*, 101(5):053918, 2007.

[4] Tariq Maqsood. Hydrothermal ZnO; mastering of lithium content and formation of palladium schottky diodes. Master's thesis, University of Oslo, 2008.

[5] L. Vines, E.V. Monakhov, and B.G. Svensson. Effect of high temperature treatments on defect centers and impurities in hydrothermally grown ZnO. *Physica B: Condensed Matter*, 404(22):4386 – 4388, 2009. Proceedings of the Third South African Conference on Photonic Materials.

[6] L. Vines, E. V. Monakhov, R. Schifano, W. Mtangi, F. D. Auret, and B. G. Svensson. Lithium and electrical properties of ZnO. *Journal of Applied Physics*, 107(10):103707, 2010.

[7] Neil W. Ashcroft and N. David Mermin. *Solid state physics*. Holt, Rinehart and Winston, 1976.

[8] Charles Kittel and Paul McEuen. *Introduction to solid state physics.* Wiley, 8 edition, 2005.

[9] Adrian P. Sutton. *Electronic structure of materials.* Clarendon Press ; New York : Oxford University Press, 1993.

[10] Richard J. D. Tilley. *Understanding solids: the science of materials.* Wiley, 2004.

[11] Truls Norby and Per Kofstad. Defects and transport in crystaline solids. Compendium used in the course "Defect Chemestry and Transportation" at the University of Oslo, September 2007.

[12] David J. Griffiths. *Introduction to quantum mechanics.* Pearson-/Prentice Hall, 2005.

[13] Stephen A. Campbell. *The science and engineering of microelectronic fabrication.* Number 2nd ed. Oxford University Press, New York, 2001.

[14] James W. Mayer and S. S. Lau. *Electronic materials science: for integrated circuits in Si and GaAs.* Macmillan, 1990.

[15] Ben G. Streetman and Sanjay Banerjee. *Solid state electronic devices.* Pearson/Prentice-Hall, 2006.

[16] P. Blood and J. W. Orton. *The electrical characterization of semiconductors: majority carriers and electron states.* Academic Press, London, 1992.

[17] R. B. Heller, J. McGannon, and A. H. Weber. Precision determination of the lattice constants of zinc oxide. *Journal of Applied Physics*, 21(12):1283–1284, 1950.

[18] K. Kihara and G. Donnay. Anharmonic thermal vibrations in ZnO. *Canadian Mineralogist*, 23(4):647, 1985.

[19] Thomas Moe Børseth. *Annealing of Ion-Implanted and As-Grown Zinc Oxide.* PhD thesis, University of Oslo, 2007.

[20] Anderson Janotti and Chris G Van de Walle. Fundamentals of zinc oxide as a semiconductor. *Reports on Progress in Physics*, 72(12):126501 (29pp), 2009.

[21] E V Monakhov, A Yu Kuznetsov, and B G Svensson. Zinc oxide: bulk growth, role of hydrogen and Schottky diodes. *Journal of Physics D: Applied Physics*, 42(15):153001 (17pp), 2009.

[22] J Nause and B Nemeth. Pressurized melt growth of ZnO boules. *Semiconductor Science and Technology*, 20(4):S45, 2005.

[23] Anderson Janotti and Chris G. Van de Walle. Native point defects in ZnO. *Physical Review B (Condensed Matter and Materials Physics)*, 76(16):165202, 2007.

[24] D. C. Look, J. W. Hemsky, and J. R. Sizelove. Residual native shallow donor in ZnO. *Phys. Rev. Lett.*, 82(12):2552–2555, Mar 1999.

[25] Tadatsugu Minami, Hirotoshi Sato, Hidehito Nanto, and Shinzo Takata. Group III Impurity Doped Zinc Oxide Thin Films Prepared by RF Magnetron Sputtering. *Japanese Journal of Applied Physics*, 24(Part 2, No. 10):L781–L784, 1985.

[26] Chris G. Van de Walle. Hydrogen as a Cause of Doping in Zinc Oxide. *Phys. Rev. Lett.*, 85(5):1012–1015, Jul 2000.

[27] E. Mollwo. Die wirkung von wasserstoff auf die leitfähigkeit und lumineszenz von zinkoxydkristallen. *Zeitschrift für Physik A Hadrons and Nuclei*, 138(3):478–488, june 1954.

[28] D. G. Thomas and J. J. Lander. Hydrogen as a donor in zinc oxide. *The Journal of Chemical Physics*, 25(6):1136–1142, 1956.

[29] A. R. Hutson. Hall effect studies of doped zinc oxide single crystals. *Phys. Rev.*, 108(2):222–230, Oct 1957.

[30] F. Tuomisto, V. Ranki, K. Saarinen, and D C. Look. Evidence of the Zn Vacancy Acting as the Dominant Acceptor in n-Type ZnO. *Phys. Rev. Lett.*, 91(20):205502, Nov 2003.

[31] Gun Hee Kim, Dong Lim Kim, Byung Du Ahn, Sang Yeol Lee, and Hyun Jae Kim. Investigation on doping behavior of copper in ZnO thin film. *Microelectronics Journal*, 40(2):272 – 275, 2009. Wide Band Gap Semiconductor Nanostructures for Optoelectronic Applications.

[32] D. C. Look, D. C. Reynolds, C. W. Litton, R. L. Jones, D. B. Eason, and G. Cantwell. Characterization of homoepitaxial p-type ZnO grown by molecular beam epitaxy. *Applied Physics Letters*, 81(10):1830–1832, 2002.

[33] L.P. Dai, H. Deng, J.J. Chen, and M. Wei. Realization of the intrinsic p-type ZnO thin film by SSCVD. *Solid State Communications*, 143(8-9):378 – 381, 2007.

[34] J. J. Lander. Reactions of lithium as a donor and an acceptor in ZnO. *Journal of Physics and Chemistry of Solids*, 15(3-4):324 – 334, 1960.

[35] M. G. Wardle, J. P. Goss, and P. R. Briddon. Theory of li in ZnO: A limitation for Li-based *p* -type doping. *Phys. Rev. B*, 71(15):155205, Apr 2005.

[36] Eun-Cheol Lee and K.J. Chang. P-type doping with group-I elements and hydrogenation effect in ZnO. *Physica B: Condensed Matter*, 376-377:707 – 710, 2006. Proceedings of the 23rd International Conference on Defects in Semiconductors.

[37] Y. J. Zeng, Z. Z. Ye, W. Z. Xu, D. Y. Li, J. G. Lu, L. P. Zhu, and B. H. Zhao. Dopant source choice for formation of p-type ZnO: Li acceptor. *Applied Physics Letters*, 88:062107, 2006.

[38] R. Schifano, E.V. Monakhov, B.G. Svensson, W. Mtangi, P. Janse van Rensburg, and F.D. Auret. Shallow levels in virgin hydrothermally grown n-type ZnO studied by thermal admittance spectroscopy. *Physica B: Condensed Matter*, 404(22):4344 – 4348, 2009. Proceedings of the Third South African Conference on Photonic Materials.

[39] R. Schifano, E. V. Monakhov, L. Vines, B. G. Svensson, W. Mtangi, and F. D. Auret. Defects in virgin hydrothermally grown n-type ZnO

studied by temperature dependent Hall effect measurements. *Journal of Applied Physics*, 106(4):043706, 2009.

[40] F. D. Auret, S. A. Goodman, M. J. Legodi, W. E. Meyer, and D. C. Look. Electrical characterization of vapor-phase-grown single-crystal ZnO. *Applied Physics Letters*, 80(8):1340–1342, 2002.

[41] H. von Wenckstern, H. Schmidt, M. Grundmann, M. W. Allen, P. Miller, R. J. Reeves, and S. M. Durbin. Defects in hydrothermally grown bulk ZnO. *Applied Physics Letters*, 91(2):022913, 2007.

[42] D. C. Look, G. C. Farlow, Pakpoom Reunchan, Sukit Limpijumnong, S. B. Zhang, and K. Nordlund. Evidence for Native-Defect Donors in n-Type ZnO. *Phys. Rev. Lett.*, 95(22):225502, Nov 2005.

[43] Dieter K. Schroder. *Semiconductor material and device characterization.* Wiley, 2006.

[44] Xiaocheng Yang and N. C. Giles. Hall effect analysis of bulk ZnO comparing different crystal growth techniques. *Journal of Applied Physics*, 105(6):063709, 2009.

[45] D. G. Brandon and Wayne D. Kaplan. *Microstructural characterization of materials.* Wiley, 1999.

[46] Knut Erik Knutsen. Investigation of zinc vacancies and their influence on N and Li related defect complexes in hydrothermal ZnO. Master's thesis, University of Oslo, 2009.

[47] Klaus Magnus Johansen. Secondary Ion Mass Spectrometry (SIMS). Lecture notes for the course MENA3100 - Material characterization, university of Oslo.

[48] J. Barbolla and S. Dueñas and L. Bailón. Admittance spectroscopy in junctions. *Solid-State Electronics*, 35(3):285 – 297, 1992.

[49] J.L. Pautrat, B. Katircioglu, N. Magnea, D. Bensahel, J.C. Pfister, and L. Revoil. Admittance spectroscopy: A powerful characterization tech-

nique for semiconductor crystals–application to znte. *Solid-State Electronics*, 23(11):1159 – 1169, 1980.

[50] Ramón Schifano. *Schottky contacts and electrical characterization of n-type hydrothermally grown ZnO*. PhD thesis, University of Oslo, 2009.

[51] Ulrike Grossner, Stig Gabrielsen, Thomas Moe Børseth, Joachim Grillenberger, Andrej Yu. Kuznetsov, and Bengt G. Svensson. Palladium Schottky barrier contacts to hydrothermally grown n-ZnO and shallow electron states. *Applied Physics Letters*, 85(12):2259–2261, 2004.

[52] R. Schifano, EV Monakhov, JS Christensen, A.Y. Kuznetsov, and BG Svensson. Schottky contacts to hydrogen doped ZnO. *physica status solidi (a)*, 205(8):1998 – 2001, 2008.

[53] E. H. Putley. *The Hall effect and related phenomena*. Butterworths, 1960.

[54] E. H. Hall. On a new action of the magnet on electric currents. *American Journal of Mathematics*, 2(3):287–292, 1879.

[55] LJ van der Pauw. A method of measuring specific resistivity and Hall effect of discs of arbitrary shape. *Philips Research Reports*, 13:1–9, 1958.

[56] Please visit `http://electron.mit.edu/~gsteele/-vanderpauw/` for this picture in it's original context.

[57] Karlheinz Seeger. *Semiconductor physics: an introduction*. Springer Series in Solid-state Sciences. Springer-Verlag Berlin and Heidelberg GmbH & Co, 9 edition, 2004.

[58] Xiaocheng Yang, Chunchuan Xu, and N. C. Giles. Role of Neutral Impurity Scattering in the Analysis of Hall Data from ZnO and Other II-VI Materials. In D.P. Norton, C. Jagadish, I. Buyanova, , and G-C. Yi, editors, *Zinc Oxide and Related Materials*, volume 1035E of *Mater. Res. Soc. Symp. Proc*, pages L04–01, 2007.

[59] L. M. Falicov and M. Cuevas. Mobility of Electrons in Compensated Semiconductors. II. Theory. *Phys. Rev.*, 164(3):1025–1032, Dec 1967.

[60] Andrea Dal Corso, Michel Posternak, Raffaele Resta, and Alfonso Baldereschi. Ab initio study of piezoelectricity and spontaneous polarization in ZnO. *Phys. Rev. B*, 50(15):10715–10721, Oct 1994.

[61] Ronald Chwang, B.J. Smith, and C.R. Crowell. Contact size effects on the van der Pauw method for resistivity and Hall coefficient measurement. *Solid-State Electronics*, 17(12):1217 – 1227, 1974.

[62] D.C. Look, H.L. Mosbacker, Y.M. Strzhemechny, and L.J. Brillson. Effects of surface conduction on Hall-effect measurements in ZnO. *Superlattices and Microstructures*, 38(4-6):406 – 412, 2005. E-MRS 2005 Symposium G: ZnO and Related Materials - Part 1.

[63] S. Graubner, C. Neumann, N. Volbers, B. K. Meyer, J. Bläsing, and A. Krost. Preparation of zno substrates for epitaxy: Structural, surface, and electrical properties. *Applied Physics Letters*, 90(4):042103, 2007.

[64] Please visit `http://www.spcgoodwill.com/catalog_f.html` for further details.

[65] Han-Ki Kim and Ji-Myon Lee. Low resistance nonalloyed Al-based ohmic contacts on n-ZnO:Al. *Superlattices and Microstructures*, 42(1-6):255 – 258, 2007. E-MRS 2006 Symposium K: ZnO and Related Materials, 2006 Spring Meeting of the European Materials Research Society.

[66] Sang-Ho Kim, Han-Ki Kim, and Tae-Yeon Seong. Effect of hydrogen peroxide treatment on the characteristics of Pt Schottky contact on n-type ZnO. *Applied Physics Letters*, 86(11):112101, 2005.

[67] R. Schifano, E. V. Monakhov, U. Grossner, and B. G. Svensson. Electrical characteristics of palladium Schottky contacts to hydrogen peroxide treated hydrothermally grown ZnO. *Applied Physics Letters*, 91(19):193507, 2007.

[68] R. Schifano, E. V. Monakhov, B. G. Svensson, and S. Diplas. Surface passivation and interface reactions induced by hydrogen peroxide treatment of n-type ZnO ($000\bar{1}$). *Applied Physics Letters*, 94(13):132101, 2009.

[69] B. K. Meyer, H. Alves, D. M. Hofmann, W. Kriegseis, D. Forster, F. Bertram, J. Christen, A. Hoffmann, M. Straßburg, M. Dworzak, U. Haboeck, and A. V. Rodina. Bound exciton and donor-acceptor pair recombinations in ZnO. *physica status solidi (b)*, 241(2):231–260, 2004.

[70] Klaus Magnus Håland Johansen. To be published.

[71] Wei-I Lee and Ruey-Ling Young. Defects and degradation in ZnO varistor. *Applied Physics Letters*, 69(4):526–528, 1996.

[72] J. C. Simpson and J. F. Cordaro. Defect clusters in zinc oxide. *Journal of Applied Physics*, 67(11):6760–6763, 1990.

[73] Muhammad Sahimi. *Applications of percolation theory*. Taylor&Francis, 1994.

[74] K Saarinen, S Hautakangas, and F Tuomisto. Positron annihilation lifetime spectroscopy of zno bulk samples. *Physical Review B*, 76(8):085202, 2007.

[75] Paul Erhart and Karsten Albe. Diffusion of zinc vacancies and interstitials in zinc oxide. *Applied Physics Letters*, 88(20):201918, 2006.

[76] M. D. McCluskey and S. J. Jokela. Defects in zno. *Journal of Applied Physics*, 106(7):071101, 2009.

[77] N. H. Nickel and K. Fleischer. Hydrogen local vibrational modes in zinc oxide. *Phys. Rev. Lett.*, 90(19):197402, May 2003.

[78] D.C. Look. Quantitative analysis of surface donors in ZnO. *Surface Science*, 601(23):5315 – 5319, 2007.

[79] D. C. Look, B. Claflin, and H. E. Smith. Origin of conductive surface layer in annealed ZnO. *Applied Physics Letters*, 92(12):122108, 2008.